PROCEEDINGS A

royalsocietypublishing.org/journal/rspa

Research

Cite this article: Cabras L, Salvadori A, Serpelloni M. 2026 A thermodynamically consistent formulation for solid-state batteries at finite strains. *Proc. R. Soc. A* **482**: 20250822. https://doi.org/10.1098/rspa.2025.0822

Received: 22 September 2025
Accepted: 13 February 2026

Subject Areas:
power and energy systems, mechanics, thermodynamics

Keywords:
electro-chemo-mechanics of materials, materials modelling and simulations, solid-state batteries, large deformation, viscoplasticity

Author for correspondence:
M. Serpelloni
e-mail: mattia.serpelloni@unibs.it

A thermodynamically consistent formulation for solid-state batteries at finite strains

L. Cabras[1,2], A. Salvadori[3] and M. Serpelloni[3]

[1]Dipartimento di Ingegneria e Architettura, Università degli Studi di Trieste, Italy
[2]Center for Energy, Environment and Transport Giacomo Ciamician, University of Trieste, Trieste, Italy
[3]Dipartimento di Ingegneria Meccanica e Industriale, Università di Brescia, Italy

AS, 0000-0002-4875-7059; MS, 0000-0003-1267-1664

This work presents a thermodynamically consistent model for all-solid-state lithium-ion batteries (ASSBs), formulated within the framework of coupled electro-chemo-mechanics of continua at finite strains. A distinctive feature of the model is the inclusion of a dual conduction mechanism within the solid electrolyte. The formulation is sufficiently general to capture the inelastic response of electrodes, whether metallic (as in viscoplastic lithium foil anodes) or porous. The mechanical behaviour of ASSBs is investigated under galvanostatic discharge conditions, accounting for both the stripping of the lithium foil—here replicated by tailored boundary conditions—and the shrinking of the porous cathode. The governing equations have been implemented in a commercial finite-element code. Numerical simulations reveal the influence of individual components on the overall cell response, identify limiting factors during charge and discharge cycles and support the optimization of cell design.

1. Introduction

Rechargeable batteries operate by converting chemical energy into electrical energy [1,2]. They are arranged in cells consisting of one positive and one negative electrode, an electrolyte for ionic transport, a separator

Electronic supplementary material is available online at https://doi.org/10.6084/m9.figshare.c.8351672.

THE ROYAL SOCIETY
PUBLISHING

to prevent short circuits caused by contact between electrodes[1] and two current collectors to transport electrons to the external circuit.[2] Currently, these devices are mainly composed of *liquid* electrolytes, which provide remarkable cycling performance, no memory, limited self-discharge, high voltage and specific capacity, and extensive temperature ranges of operation [4]. However, these systems are also highly flammable, eventually leading to thermal runaway. Consequently, new technologies are expected to replace liquid electrolytes in the next generation of batteries [5]. All-solid-state lithium-ion batteries (ASSBs) are touted as possible candidates with the potential to increase the energy density using a lithium anode, limit degradation processes [6–8], ensure thermal and electrochemical stability and prevent hazardous liquid leaks [9–11]. Despite these promising features, ASSBs still present a variety of chemo-mechanical issues, as pointed out extensively in [6], mainly because of poor solid–solid interfacial contact and limited ionic conductivity [3]. Particularly, the mechanical behaviour of solid electrolytes is brittle and can cause microfractures that affect stability and compatibility with electrode interfaces and raise interfacial resistance [12]. Dendritic development [13], which is acknowledged as the main cause of battery short-circuits, is encouraged by microstructural defects such as pores, fractures and grain boundaries [14–16]. For these reasons, further enhancements are sought with the aim of improving the contact between the electrode and the solid electrolyte as well as the fracture toughness of the electrolyte, both of which are critical to the structural integrity of the system. The solid-state electrolyte, which is the key component of this technology, could be broadly classified as organic (mainly solid polymers [17]) and inorganic (glasses [18], or ceramic [19] oxides or sulfides) [3]. In particular, this manuscript focuses on a specific class of inorganic solid electrolyte known as lithium phosphorus oxynitride, or LiPON. This type of electrolyte shows an amorphous glass ceramic structure wherein lithium is bound to the non-bridging oxygen atoms [18]. LiPON is characterized by two mechanisms of ionic conduction [20]. In ASSBs, LiPON is paired with a pure metal lithium negative electrode and a $LiCoO_2$ positive intercalation[3] electrode [22,23]. In solid electrolytes at standard conditions, thermal activation promotes lithium ions to mobile states, creating vacancies carrying an effective negative charge where lithium ions have been excited. Following the single-ion conduction approach common in the literature [20,24], these vacancies are modelled as fixed. This assumption ensures a uniform Li-ion distribution throughout the electrolyte to satisfy electroneutrality [20,25]. In the absence of a concentration gradient to drive ionic flux, these models simplify to an essentially ohmic description of transport [20]. More recent developments, [20,26] among others, have seen single-ion conduction models superseded by dual-mechanism frameworks. These offer a more high-fidelity representation of ionic mobility in solid electrolytes by accounting for both lattice hopping and interstitial diffusion [20]. The proposed LiPON model accounts for both hopping and interstitial mechanisms, as well as their interactions during battery operation [20,27]. Specifically, the present work represents a significant step forward by extending the one-dimensional (1D) formulation for LiPON [20] into a fully coupled three-dimensional (3D) thermodynamically consistent framework. This advancement enables the investigation of complex cathode architectures, such as 3D-structured or architected electrodes, that 1D or simplified two-dimensional (2D) models are unable to resolve, particularly when integrated into a comprehensive full-battery cell formulation. Furthermore, the model considers the dynamic exchange between ions and vacancies, where the motion of positive ions inherently creates new vacant sites. In this context, only the positive ions are mobile, whereas the resulting concentration of negative vacancies is not assumed *a priori* but emerges from the coupled governing equations. Specifically, a simplified single-ion model treats ionic conductivity as a macroscopic material constant, effectively masking the underlying site-occupancy dynamics. In contrast, by decoupling hopping and interstitial transport, the current model accounts for

---

[1] In solid-state batteries, the electrolyte itself performs as the separator.

[2] In the case of pure metal anode, e.g. lithium metal foil, the electrode acts as a collector [3].

[3] Intercalation is a reversible mechanism characterized by the introduction of a mobile ion or molecule into interstitial positions within a crystal lattice. In particular, the layered crystal structures [21] of $LiCoO_2$ favour the reversible intercalation of lithium, which moves among the 2D layers [3].

the limited availability of non-bridging oxygen sites. This distinction is crucial because the two mechanisms possess different activation energies and mobilities.

(a) Aims of the work

ASSBs are characterized by an intrinsic multiscale and multiphysics nature. In this manuscript, we aim to investigate how mechanics affects battery operation via multiphysics modelling concepts, methodologies and simulations [3]. Mechanics is essential for battery operation and regulates multiple internal processes, including the swelling and shrinking of the porous cathode during charge and discharge cycles [28,29], lithium plating and stripping [30] on the surface of the metallic anode, in contact with the electrolyte, the dendrite formation within the solid electrolyte [31] and its effect on ionic conductivity [32]. Collectively, these processes concur in promoting the ageing [33] of the battery cell. In particular, numerical outcomes will show how to guide the customization of the design, providing valuable insights into the electrochemical response of the cell during operation and predicting limiting factors during charge and discharge cycles.

(i) Theoretical insights

To fully describe this type of battery, an electro-chemo-mechanical model, grounded in the realm of continuum thermodynamics, has been developed. The formulation is thermodynamically consistent and multiscale-compatible, which is found to be relevant for porous cathodes [34–36]. The electrochemical response of the cell has been combined with the mechanical one, resulting in a thorough explanation of the behaviour of this new generation of batteries. To describe the mechanical response of the metallic lithium employed in the anode, the formulation introduced in [37] and followed by more recent papers [38,39] on large elastic-viscoplastic deformations of metals, has been adopted. The proposed multiphysics framework is wide-ranging and can be applied to various types of cells.

(ii) Numerical insights

A numerical description of the model has been fully developed, adopting a planar geometry (2032-type coin cell assembly) as schematically depicted in figure 1. Numerical simulations provide valuable insights into the electrochemical response of the cell during operation, as well as predictions of limiting parameters during charge/discharge cycles. Furthermore, we concentrate on the cathode design, inspired by the possibilities provided by newer 2D printing technologies, which allow the construction of atypical 3D batteries with flexible designs such as microscale 3D shapes, innovative 3D grid-patterned $LiFePO_4@MgO$ composite electrodes [40], 3D patterned self-supported thick electrodes for high-areal-energy and high-power-density lithium-ion batteries [41]. In [42], 3D printing has been employed with $\mathrm{Li_{1.3}Al_{0.3}Ti_{1.7}(PO_4)_3}$ (LATP)-based inks to create ceramic and hybrid solid-state electrolytes with arbitrary forms and high conductivities.

The multiphysics model formulation, complemented by a simulation-based approach may equip researchers with new tools for observing interconnected and complex reality. Specifically, the present continuum scale model has the ability to link and highlight the nonlinear interactions between the many physical observables, including electric potential, species concentrations and displacements [3,18,43,44].

(iii) The paper is organized as follows

In §2, preliminary concepts pertinent to continuum thermodynamics have been summarized, providing the theoretical background necessary to derive the balance equations for ASSBs in the realm of finite strains, see §2d. The fundamental statements for the physical modelling of the solid electrolyte, of the porous electrode, and of the lithium foil are described in §3a,b,c, respectively. Governing equations have been numerically implemented in COMSOL Multiphysics, and the simulation of the discharge of an entire cell has been carried out via the finite-element method in

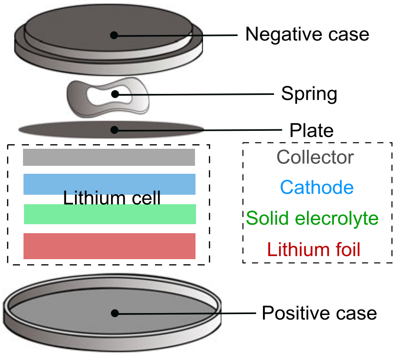

Figure 1. A pictorial view of an all-solid-state electrochemical cell.

§4. Outcomes are profoundly discussed, and a parametric study on the geometrical configuration of the cathode has been performed before drawing conclusions and further developments, see §5.

This work extends the content of [26,29] to the realm of all solid-state batteries at finite strains, with an visco-plastic response of lithium foils providing insights into the issue of constrained deposition, and a double conduction mechanism in the electrolyte. The proposed framework serves, among other purposes, as a predictive tool for the design of architected electrodes; although not directly compared with experimental data in this study, it could establish a theoretical basis for future experimental validation and optimization of solid-state battery architectures.

2. Preliminary concepts

(a) Notation

We adopt uppercase fonts to denote referential $\overrightarrow{VECTOR}$ and $\boldsymbol{TENSOR}$ fields, whereas lowercase fonts define $\overrightarrow{vector}$ and $\boldsymbol{tensor}$ quantities in the current configuration. As in [45], scalar fields are identified by lowercase typefaces, with a subscript $_R$ for referential fields. Specific symbols are used for linear operators, such as '$\cdot$' for the scalar product between two vectors or tensors, '$\times$' for the cross product of two vectors and '$\otimes$' for tensor product, respectively. We denote with $\partial\square/\partial t$ and $\mathrm{d}\square/\mathrm{d}t$ the partial and total time derivatives, respectively. To favour readability, the total time derivative will be sometimes denoted with a 'dot above' notation, i.e.

$$\frac{\mathrm{d}\square}{\mathrm{d}t} = \dot{\square}.$$

(b) Kinematics

A battery cell is conceived as the union of its components, modelled as continua embedded in the Euclidean space $\mathbb{R}^3$. Let $\mathcal{B}_t \in \mathbb{R}^3$ be the spatial characterization of a generic advecting component. Its initial configuration $\mathcal{B}_{t=0}$ is assumed to coincide with the reference configuration $\mathcal{B}_R$ (see figure 2); $\partial\mathcal{B}_t$ and $\partial\mathcal{B}_R$ denote the spatial and referential boundaries, respectively.

A point $\vec{X} \in \mathcal{B}_R$ at a given instant t is relocated at position $\vec{x}(\vec{X}, t) \in \mathcal{B}_t$ by means of a smooth motion map $\vec{\chi}$ (see [45]), i.e.

$$\vec{x} = \vec{\chi}(\vec{X}, t) \qquad \text{such that} \qquad \vec{X} = \vec{\chi}(\vec{X}, 0).$$

Denote as usual with $\boldsymbol{F} = \partial\vec{x}/\partial\vec{X}$ the deformation gradient, and with $J = \det[\boldsymbol{F}] > 0$ its determinant. Let $\mathcal{P}_t \subset \mathcal{B}_t$ be an arbitrary sub-region in the current configuration and $\mathcal{P}_R \subset \mathcal{B}_R$ its referential

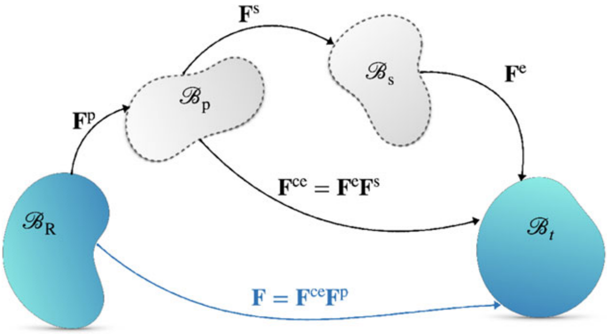

Figure 2. The reference $\mathcal{B}_R$ and current $\mathcal{B}_t$ configurations, depicted together with the intermediate configurations generated by the multiplicative decomposition of the deformation gradient [46].

image. To any scalar, vector or tensor field $a(\vec{x},t)$ the transformation rule

$$\int_{\mathcal{P}_t} a(\vec{x},t)\,\mathrm{d}v = \int_{\mathcal{P}_R} J(\vec{X},t)a(\vec{\chi}(\vec{X},t),t)\,\mathrm{d}V \tag{2.1}$$

applies, and $A(\vec{X},t) = J(\vec{X},t)a(\vec{\chi}(\vec{X},t),t)$ is the referential counterpart of $a(\vec{x},t)$.

Denote with

$$\vec{v}_{\mathrm{adv}}(\vec{x},t) = \frac{\mathrm{d}\vec{x}}{\mathrm{d}t}$$

the velocity of advection at $\vec{x}$. The kinematic definition[4] of the molar flux of any species α flowing in $\mathcal{B}_t$ will be expressed as

$$\vec{h}_\alpha(\vec{x},t) = c_\alpha(\vec{v}_\alpha - \vec{v}_{\mathrm{adv}}),$$

in terms of the concentration field $c_\alpha(\vec{x},t)$ and the species velocity $\vec{v}_\alpha(\vec{x},t)$.[5] The transformation rule

$$\int_{\partial\mathcal{P}_t} \vec{h}_\alpha(\vec{x},t)\cdot\vec{n}\,\mathrm{d}a = \int_{\partial\mathcal{P}_R} \vec{H}_\alpha(\vec{X},t)\cdot\vec{N}\,\mathrm{d}A \tag{2.2}$$

holds, where the referential molar flux of species α,

$$\vec{H}_\alpha(\vec{X},t) = J(\vec{X},t)\,\boldsymbol{F}^{-1}\,\vec{h}_\alpha(\vec{x}(\vec{X},t),t),$$

emanates from Nanson's formula $\vec{n}\,\mathrm{d}a = J(\vec{X},t)\,\vec{\boldsymbol{F}}^{-\mathrm{T}}\,\vec{N}\,\mathrm{d}A$.

The differential operators *divergence*, *gradient*, *curl* and *Laplacian* are denoted, respectively, with capital letters as Div[], Grad [], Curl [] and Lapl[] in $\mathcal{B}_R$ and with div[], grad [], curl [] and lapl[] in the current configuration.

During battery operation, electrochemical processes intertwine with thermal evolution, transport of species and mechanical stress generation. To address these couplings, the explicit form of the constitutive prescriptions is derived by focusing on adiabatic and isothermal processes. To further account for the multiphysics nature of charge–discharge, under the hypothesis of thermal equilibrium, the deformation gradient $\boldsymbol{F}$ has been decomposed (as in [46]):

$$\boldsymbol{F} = \boldsymbol{F}^e\boldsymbol{F}^s\boldsymbol{F}^p = \boldsymbol{F}^{ce}\boldsymbol{F}^p. \tag{2.3}$$

Specifically, $\boldsymbol{F}^p$ models the flow of defects, which trigger plastic or visco-plastic deformations—see [45]; $\boldsymbol{F}^e$ describes the local reversible elastic deformation and $\boldsymbol{F}^s$ the local volumetric swelling (or shrinking) caused by the presence of a guest species in a host material [49]. The chemo-elastic

---

[4] See the electronic supplementary material—*§1: The kinematic definition of the molar flux*—for in-depth discussions.

[5] Following the theoretical framework established in [47,48], $\vec{v}_\alpha$ denotes the velocity of species α, which is distinct from the velocity of the host material $\vec{v}_{\mathrm{adv}}$. This allows for the definition of the relative molar flux $\vec{h}_\alpha$ used in the balance equations.

deformation gradient $\boldsymbol{F}^{ce}$ is defined by comparison in equation (2.3) and we define its determinant as $J^{ce} = \det(\boldsymbol{F}^{ce})$. We assume that volumetric swelling is isotropic, i.e.

$$\boldsymbol{F}^{s} = \lambda_{s}\mathbf{1},$$

whence $J^{s} = \det(\boldsymbol{F}^{s}) = \lambda_{s}^{3}$. As usual, the plastic flow is assumed to be isochoric, i.e. $J^{p} = \det(\boldsymbol{F}^{p}) = 1$.

(c) Internal power expenditure

In view of the decomposition equation (2.3), the localized internal power expenditure can be expressed as

$$\boldsymbol{P} \cdot \dot{\boldsymbol{F}} = J^{p}\frac{1}{2}\boldsymbol{S}^{ce} \cdot \dot{\boldsymbol{C}}^{ce} + J^{p}\boldsymbol{M}^{ce} \cdot \boldsymbol{l}^{p}, \tag{2.4}$$

where:

(i) $\boldsymbol{P}$ is the first Piola–Kirchhoff stress tensor;
(ii) $\boldsymbol{S}^{ce} = J^{ce}\boldsymbol{F}^{ce^{-1}}\boldsymbol{\sigma}\boldsymbol{F}^{ce^{-\mathrm{T}}}$ is the second Piola–Kirchhoff chemo-elastic stress tensor;[6]
(iii) $\boldsymbol{C}^{ce} = \boldsymbol{F}^{ce^{\mathrm{T}}}\boldsymbol{F}^{ce}$ is the right Cauchy–Green chemo-elastic strain tensor;
(iv) $\boldsymbol{M}^{ce} = J^{ce}\boldsymbol{F}^{ce^{\mathrm{T}}}\boldsymbol{\sigma}\boldsymbol{F}^{ce^{-\mathrm{T}}} = \boldsymbol{C}^{ce}\boldsymbol{S}^{ce}$ is the Mandel chemo-elastic stress tensor;
(v) $\boldsymbol{l}^{p} = \dot{\boldsymbol{F}}^{p}\boldsymbol{F}^{p^{-1}}$ is the visco-plastic velocity gradient; $\boldsymbol{l}^{p}$ is commonly decomposed in symmetric and skew-symmetric parts as follows: $\boldsymbol{l}^{p} = \boldsymbol{d}^{p} + \boldsymbol{w}^{p}$, where $\boldsymbol{w}^{p} = \mathbf{0}$.

(d) Referential balance equations

In the approach named after Larché–Cahn [50,51], species α flow into a hosting lattice, which is solely responsible for load-bearing capacity and has a time invariant referential density ρ_{R}^{H}, i.e.

$$\frac{\partial \rho_{\mathrm{R}}^{H}}{\partial t} = 0. \tag{2.5a}$$

Mass balance equations describe the spatial and temporal variations of referential concentrations c_{R}^{α} as

$$\frac{\partial c_{\mathrm{R}}^{\alpha}}{\partial t} + \mathrm{Div}[\vec{H}_{\alpha}] + r_{\mathrm{R}}^{\alpha} = 0, \tag{2.5b}$$

where r_{R}^{α} are chemical reaction rates. Equations (2.5)[7] will be specialized for each battery component in the remainder of the paper.

Neglecting the inertia forces of the hosting material and the flowing species [47,48], the *balances of linear and angular momentum* read

$$\mathrm{Div}[\boldsymbol{P}] + \vec{B} = \vec{0} \tag{2.6}$$

and

$$\boldsymbol{F}\boldsymbol{P}^{T} = \boldsymbol{P}\boldsymbol{F}^{T}, \tag{2.7}$$

where vector $\vec{B}$ accounts for the referential body forces. Some authors [47] express the Piola–Kirchhoff stress as the sum of mechanical, chemical and Maxwell tensors. In this manuscript every contribution arises naturally from the Helmholtz free-energy, as in [52].

Maxwell's equations [25,53,54] can be applied to batteries in their electro-quasi-static conditions, except for two boundary layers [55,56]. The *charge balance equation* will be thus written

---

[6] The use of the term 'chemo-elastic' is intended to specify that $\mathbf{S}^{ce}$ is the second Piola–Kirchhoff stress tensor mapped to the intermediate configuration defined by $\mathbf{F}^{ce}$. This logic extends to both the first Piola–Kirchhoff stress $\mathbf{P}^{ce}$ and the Mandel stress tensor $\mathbf{M}^{ce}$, the latter of which drives dissipation within the same intermediate state.

[7] See the electronic supplementary material—§2: *Mass balance equations*—for an in-depth discussion on the pull-back of the mass balance equations from the current configuration to the reference one.

applying the divergence operator to Ampére's law (with Maxwell's correction),[8] i.e.

$$\mathrm{Div}\left[\frac{\mathrm{d}}{\mathrm{d}t}\vec{D}+\vec{I}\right]=0. \tag{2.8}$$

Vectors $\vec{D}$ and $\vec{I}$ are the referential electric displacement field and the current density, respectively. For electric conductors, equation (2.8) simplifies as

$$\mathrm{Div}[\vec{I}]=0. \tag{2.9}$$

The current density into the electrolyte is due to ionic motion, which in turn may promote a referential charge density q_R. Faraday's electrolysis law reads

$$q_R=F\sum_{\alpha} z_\alpha c_{\mathrm{R}}^{\alpha} \quad \text{and} \quad \vec{I}=F\sum_{\alpha} z_\alpha \vec{H}_\alpha, \tag{2.10}$$

having denoted Faraday's constant with F and the ionic valence of species with z_α.

As discussed fully in [25,57], stemming from fundamental balance equations grants thermodynamic consistency and makes the formulation suitable for multiscale homogenization strategies. Different approaches, such as the family of Newman's models [58], stem from the electro-neutrality condition. They will not be discussed in this work.

(e) Thermodynamic prescriptions

We denote with $\mathit{\Gamma}_{Rj}$ the jth referential state variable and with $\psi_{\mathrm{R}}(\mathit{\Gamma}_{Rj})$ the referential Helmholtz free energy. We further denote with λ_{Rj} a referential generalized variable, which is either energy or entropy conjugated to $\mathit{\Gamma}_{Rj}$. A general form of the Clausius–Duhem inequality can be stated as

$$\sum_j\left(\lambda_{Rj}-\frac{\partial\psi_{\mathrm{R}}}{\partial\mathit{\Gamma}_{Rj}}\right)\cdot\frac{\mathrm{d}}{\mathrm{d}t}\mathit{\Gamma}_{Rj}-\sum_k \mathrm{J}_{\mathrm{R}k}\cdot\mathrm{Y}_{\mathrm{R}k}\geq 0, \tag{2.11}$$

where the second sum is the inner product of the referential thermodynamic fluxes $\mathrm{J}_{\mathrm{R}k}$ and forces $\mathrm{Y}_{\mathrm{R}k}$ [59–62]. All terms will be specified in the next section for each battery component. Relying on the Coleman–Noll procedure [63,64], one writes the constitutive prescriptions as

$$\lambda_{Rj}=\frac{\partial\psi_R}{\partial\mathit{\Gamma}_{Rj}}. \tag{2.12}$$

The inequality constraint

$$\sum_k \mathrm{J}_{\mathrm{R}k}\cdot\mathrm{Y}_{\mathrm{R}k}\leq 0 \tag{2.13}$$

is satisfied by the Fick's, Fourier's, and Ohm's laws [59,65] by relating the thermodynamic fluxes to the gradient of an intensive property[9] ω_k

$$\vec{J}_{\mathrm{R}_k}=-\mathbf{K}_{\mathrm{R}}\mathrm{Grad}\,[\omega_k] \tag{2.14}$$

through a positive-definite matrix $\mathbf{K}_{\mathrm{R}}$, which simplifies in $\mathbf{K}_{\mathrm{R}}=k_{\mathrm{R}}\mathbf{1}$ and $k_{\mathrm{R}}>0$ under the isotropy assumption. This approach will be considered in the rest of the paper. The linear relation equation (2.14) has been written by some authors [66,67] in the current configuration, leading to a geometrical dependence $\mathbf{K}_{\mathrm{R}}=kJ(\vec{X},t)\boldsymbol{C}^{-1}$ of the matrix $\mathbf{K}_{\mathrm{R}}$.

In [25], foundations for the electro-quasi-static model [68] in Li-ion batteries have been presented, which will be assumed henceforth as an approximation of the full Maxwell's equations set. In the framework of electro-quasi-statics, the time derivative of the magnetic potential is

---

[8] See the electronic supplementary material—§3: *Maxwell's Equations*.

[9] Which specifies the chemical potential (μ), the temperature (T) and the electric potential (ϕ).

neglected. Accordingly, the electric field reads

$$\vec{E} = -\mathrm{Grad}\,[\phi] \tag{2.15}$$

and Maxwell-Faraday's law simply states that $\vec{E}$ is irrotational. It is usual in the electro-mechanics community [47,66,67] to linearly relate the electric displacement $\vec{d}$ and the electric field $\vec{e}$ in the current configuration, by means of a quadratic form of the spatial Helmholtz free energy $\psi^{\mathrm{es}} = \psi_{\mathrm{R}}^{\mathrm{es}}/J$. We will follow such approach, too.

The referential Helmholtz free-energy density ψ_{R} will be decomposed in the rest of the paper as

$$\psi_{\mathrm{R}} = \psi_{\mathrm{R}}^{0} + \psi_{\mathrm{R}}^{\mathrm{mec}} + \psi_{\mathrm{R}}^{\mathrm{mix}} + \psi_{\mathrm{R}}^{\mathrm{es}} + \psi_{\mathrm{R}}^{\mathrm{in}}, \tag{2.16}$$

where: (i) ψ_{R}^{0} is the standard Helmholtz free energy, (ii) $\psi_{\mathrm{R}}^{\mathrm{mec}}$ the free energy associated with the mechanical deformation of the host material, (iii) $\psi_{\mathrm{R}}^{\mathrm{mix}}$ the free energy accounting for the interactions between the species and host material, (iv) $\psi_{\mathrm{R}}^{\mathrm{es}}$ the free energy owing to the electrostatic contribution, and (v) $\psi_{\mathrm{R}}^{\mathrm{in}}$ the free energy related to an inelastic response of the material (viscous or plastic).

3. Specifications

(a) Solid electrolyte

Our model accounts for two ionic conduction mechanisms, as recently published for LiPON in [18] and observed in garnet solid electrolytes [8]. LiPON's structure is amorphous, with the (ionic) lithium bound to the non-bridging oxygen atoms (LiO). In standard conditions, some of the Li-ions (Li^+) are thermally excited, and the chemical ionization reaction

$$\mathrm{LiO} \underset{k_b^1}{\overset{k_f^1}{\rightleftarrows}} \mathrm{Li}^+ + \mathrm{n}^- \tag{3.1}$$

occurs, letting uncompensated negative charge (n^-) associated with a vacancy in the LiPON matrix. Most of the Li^+ generated via equation (3.1) hop and fill a nearby vacancy. Some of the Li^+ ions, denoted with $\mathrm{Li}^+_{\mathrm{int}}$, move in a meta-stable interstitial state

$$\mathrm{Li}^+ \underset{k_b^2}{\overset{k_f^2}{\rightleftarrows}} \mathrm{Li}^+_{\mathrm{int}}, \tag{3.2}$$

and the reaction equation (3.2) determines how many of these ions are in the interstitial state. As a consequence, Li^+ and $\mathrm{Li}^+_{\mathrm{int}}$ are the only ionic species permitted to flow, and therefore Faraday's law of electrolysis equation (2.10)-B reduces to

$$\vec{I} = F(z_{\mathrm{Li}^+}\vec{H}_{\mathrm{Li}^+} + z_{\mathrm{Li}^+_{\mathrm{int}}}\vec{H}_{\mathrm{Li}^+_{\mathrm{int}}}).$$

The mass balance equation (2.5*b*) specializes for each species as

$$\frac{\partial}{\partial t}c_R^{\mathrm{LiO}} + \mathrm{w}^1_{\mathrm{R}} = 0 \tag{3.3a}$$

$$\frac{\partial}{\partial t}c_R^{\mathrm{Li}^+} + \mathrm{Div}[\vec{H}_{\mathrm{Li}^+}] - \mathrm{w}^1_{\mathrm{R}} + \mathrm{w}^2_{\mathrm{R}} = 0 \tag{3.3b}$$

$$\frac{\partial}{\partial t}c_R^{\mathrm{Li}^+_{\mathrm{int}}} + \mathrm{Div}[\vec{H}_{\mathrm{Li}^+_{\mathrm{int}}}] - \mathrm{w}^2_{\mathrm{R}} = 0 \tag{3.3c}$$

and

$$c_R^{\mathrm{Li}_0} + c_R^{\mathrm{n}^-} = c_0. \tag{3.3d}$$

The reaction rates $\mathrm{w}^1_{\mathrm{R}}$ and $\mathrm{w}^2_{\mathrm{R}}$ are related to the concentrations via the mass action law, as [46,62,69]

$$\mathrm{w}^1_{\mathrm{R}} = k^1_{f_{\mathrm{R}}}\frac{\theta_{\mathrm{R}}^{\mathrm{LiO}}}{1-\theta_{\mathrm{R}}^{\mathrm{LiO}}} - k^1_{b_{\mathrm{R}}}\frac{\theta_{\mathrm{R}}^{\mathrm{n}^-}}{1-\theta_{\mathrm{R}}^{\mathrm{n}^-}}\frac{\theta_{\mathrm{R}}^{\mathrm{Li}^+}}{1-\theta_{\mathrm{R}}^{\mathrm{Li}^+}} \tag{3.4a}$$

and

$$\mathrm{w}^2_{\mathrm{R}} = k^2_{f_{\mathrm{R}}} \frac{\theta_{\mathrm{R}}^{\mathrm{Li}^+}}{1-\theta_{\mathrm{R}}^{\mathrm{Li}^+}} - k^2_{b_{\mathrm{R}}} \frac{\theta_{\mathrm{R}}^{\mathrm{Li}^+_{\mathrm{int}}}}{1-\theta_{\mathrm{R}}^{\mathrm{Li}^+_{\mathrm{int}}}}, \tag{3.4b}$$

where $\theta^{\alpha}_{\mathrm{R}} = c^{\alpha}_{\mathrm{R}}/\bar{c}^{\alpha}_{\mathrm{R}}$ and $\bar{c}^{\alpha}_{\mathrm{R}}$ is the saturation concentration [56] of ionic species in the hosting material. Moreover, the factors $k^{1,2}_{f_{\mathrm{R}}}$ and $k^{1,2}_{b_{\mathrm{R}}}$ in equations (3.4) are the forward and backward rate constants of the chemical reactions equations (3.1)–(3.2).[10]

The state variables for the LiPON electrolyte are $\Gamma_{\mathrm{R}} = \{T, \boldsymbol{C}, c_{R}^{\mathrm{LiO}}, c_{R}^{\mathrm{Li}^+}, c_{R}^{\mathrm{Li}^+_{\mathrm{int}}}, c_{R}^{\mathrm{n}^-}, \vec{D}\}$. Following the rigorous approach developed in [46,55,69] and summarized in the electronic supplementary material - *§3: Thermodynamics for a Larché–Cahn system*, the Clausius–Duhem inequality equation (2.11), under the assumption of thermal equilibrium, takes the form:

$$\sum_{\alpha}\left(\mu_{\alpha} - \frac{\partial \psi_{\mathrm{R}}}{\partial c^{\alpha}_{\mathrm{R}}}\right)\frac{\partial c^{\alpha}_{\mathrm{R}}}{\partial t} - \left(\frac{\partial \psi_{\mathrm{R}}}{\partial T} + \eta_{\mathrm{R}}\right)\frac{\partial T}{\partial t} + \left(\frac{\boldsymbol{S}}{2} - \frac{\partial \psi_{\mathrm{R}}}{\partial \boldsymbol{C}}\right)\cdot\frac{\partial \boldsymbol{C}}{\partial t} + \left(\vec{E} - \frac{\partial \psi_{\mathrm{R}}}{\partial \vec{D}}\right)\cdot\frac{\partial \vec{D}}{\partial t}$$
$$+\,\mathrm{w}^1_{\mathrm{R}}\mathrm{A}^1_{\mathrm{R}} - \mathrm{w}^2_{\mathrm{R}}\mathrm{A}^{\,2}_{\,\mathrm{R}} - \mathrm{Grad}\,[\bar{\mu}_{\mathrm{Li}^+}]\cdot\vec{H}_{\mathrm{Li}^+} - \mathrm{Grad}\,[\bar{\mu}_{\mathrm{Li}^+_{\mathrm{int}}}]\cdot\vec{H}_{\mathrm{Li}^+_{\mathrm{int}}} \geq 0. \tag{3.6}$$

Index α in equation (3.6) and in the rest of the electrolyte section extends over the four species LiO, Li^+, $\mathrm{Li}^+_{\mathrm{int}}$, n^-. The electrochemical potential is defined as usual as

$$\bar{\mu}_{\alpha} = \mu_{\alpha} + F z_{\alpha}\phi.$$

Chemical affinities are defined as

$$\mathrm{A}^1_{\mathrm{R}} = -\mu_{\mathrm{LiO}} + \mu_{\mathrm{Li}^+} + \mu_{\mathrm{n}^-}$$

and

$$\mathrm{A}^2_{\mathrm{R}} = -\mu_{\mathrm{Li}^+} + \mu_{\mathrm{Li}^+_{\mathrm{int}}}.$$

Applying the Coleman–Noll procedure, the constitutive prescriptions equation (2.12) are specified as

$$\eta_{\mathrm{R}} = -\frac{\partial \psi_{\mathrm{R}}}{\partial T}, \quad \boldsymbol{S} = 2\frac{\partial \psi_{\mathrm{R}}}{\partial \boldsymbol{C}}, \quad \vec{E} = \frac{\partial \psi_{\mathrm{R}}}{\partial \vec{D}}, \; \mu_{\alpha} = \frac{\partial \psi_{\mathrm{R}}}{\partial c^{\alpha}_{\mathrm{R}}} \tag{3.7}$$

and in view of Curie's principle [62,70], the inequality (2.13) splits as

$$\mathrm{w}^1_{\mathrm{R}}\mathrm{A}^{\,1}_{\,\mathrm{R}} + \mathrm{w}^2_{\mathrm{R}}\mathrm{A}^{\,2}_{\,\mathrm{R}} \leq 0 \tag{3.8a}$$

and

$$\mathrm{Grad}\,[\bar{\mu}_{\mathrm{Li}^+}]\cdot\vec{H}_{\mathrm{Li}^+} + \mathrm{Grad}\,[\bar{\mu}_{\mathrm{Li}^+_{\mathrm{int}}}]\cdot\vec{H}_{\mathrm{Li}^+_{\mathrm{int}}} \leq 0. \tag{3.8b}$$

Solid electrolytes are usually brittle and do not show swelling during ionic motion. Hence $\psi^{\mathrm{in}}_{\mathrm{R}} = 0$ and $\boldsymbol{F}^s = \boldsymbol{F}^p = \mathbf{1}$. Accordingly, $\boldsymbol{F} = \boldsymbol{F}^e$ and the following additive decomposition (see equation (2.16)) of the Helmholtz free energy,

$$\psi_{\mathrm{R}} = \underbrace{\mu^{\alpha}_{0}c^{\alpha}_{\mathrm{R}}}_{\psi^{0}_{\mathrm{R}}} + \underbrace{\mathrm{RT}\,\bar{c}^{\alpha}_{\mathrm{R}}[\theta^{\alpha}_{\mathrm{R}}\ln(\theta^{\alpha}_{\mathrm{R}}) + (1-\theta^{\alpha}_{\mathrm{R}})\ln(1-\theta^{\alpha}_{\mathrm{R}})]}_{\psi^{\mathrm{mix}}_{\mathrm{R}}} + \underbrace{\frac{\vec{D}\cdot\boldsymbol{C}\vec{D}}{2\epsilon J}}_{\psi^{\mathrm{es}}_{\mathrm{R}}} + \underbrace{\mathrm{G}\boldsymbol{E}\cdot\boldsymbol{E} + \frac{\lambda}{2}\mathrm{tr}[\boldsymbol{E}]^2}_{\psi^{\mathrm{mec}}_{\mathrm{R}}}, \tag{3.9}$$

is adopted in the solid electrolyte, with R the universal gas constant. The mixing free energy $\psi^{\mathrm{mix}}_{\mathrm{R}}$ has a purely entropic nature, since no phase segregation is noticed in solid electrolytes. The mechanical free energy has a Saint Venant–Kirchhoff elastic origin, with λ the Lamé constant and

---

[10] Based on [18,46] and the Arrhenius equation, the rate constants are considered to be a function of the electric potential, as expressed below:

$$k^{1,2}_{f_{\mathrm{R}}} = k^{1,2}_{f_{\mathrm{R}0}}\exp\left(\frac{\zeta F\phi}{RT}\right), \quad \mathrm{k}^{1,2}_{b_{\mathrm{R}}} = \mathrm{k}^{1,2}_{b_{\mathrm{R}0}}\exp\left(\frac{\zeta F\phi}{RT}\right). \tag{3.5}$$

Here, ζ represents an amplification factor. It is important to note that the electric potential does not affect the equilibrium constants; rather, it influences the chemical kinetics without altering the equilibrium states [18].

G the shear modulus. Finally, the electrostatic free energy is the referential representation of the spatial quadratic form

$$\psi^{\mathrm{es}} = \frac{\vec{d} \cdot \vec{d}}{2\epsilon},$$

where ϵ is the electrical permittivity [47,67].

In view of the selection equation (3.9) of the Helmholtz free energy, simple algebra leads to the constitutive equations:

$$\vec{D} = -\epsilon J \boldsymbol{C}^{-1} \mathrm{Grad}\,[\phi], \tag{3.10}$$

$$\boldsymbol{S} = \lambda \mathrm{tr}[\boldsymbol{E}]\mathbf{1} + 2G\boldsymbol{E} + \frac{1}{2\epsilon J}\{2\vec{D} \otimes \vec{D} - [\vec{D} \cdot (\boldsymbol{C}\vec{D})]\boldsymbol{C}^{-1}\}, \tag{3.11}$$

$$\overline{\mu}_{\mathrm{Li}^+_{\mathrm{int}}} = \mu_0^{\mathrm{Li}^+_{\mathrm{int}}} + \mathrm{RT}\ln\left[\frac{\theta_{\mathrm{R}}^{\mathrm{Li}^+_{\mathrm{int}}}}{1-\theta_{\mathrm{R}}^{\mathrm{Li}^+_{\mathrm{int}}}}\right] + F\phi, \tag{3.12}$$

$$\overline{\mu}_{\mathrm{Li}^+} = \mu_0^{\mathrm{Li}^+} + \mathrm{RT}\ln\left[\frac{\theta_{\mathrm{R}}^{\mathrm{Li}^+}}{1-\theta_{\mathrm{R}}^{\mathrm{Li}^+}}\right] + F\phi, \tag{3.13}$$

$$\mu_{\mathrm{LiO}} = \mu_0^{\mathrm{LiO}} + \mathrm{RT}\ln\left[\frac{\theta_{\mathrm{R}}^{\mathrm{LiO}}}{1-\theta_{\mathrm{R}}^{\mathrm{LiO}}}\right] \tag{3.14}$$

and

$$\overline{\mu}_{\mathrm{n}^-} = \mu_0^{\mathrm{n}^-} + \mathrm{RT}\ln\left[\frac{\theta_{\mathrm{R}}^{\mathrm{n}^-}}{1-\theta_{\mathrm{R}}^{\mathrm{n}^-}}\right] - F\phi. \tag{3.15}$$

The contribution in brackets to the second Piola–Kirchhoff in equation (3.11) is the so-called Maxwell tensor. To comply with the constitutive constraint given by the Clausius–Duhem inequality equation (3.8b), we adopt the following Fickian type law [46,69,71]:

$$\vec{H}_\alpha = -\mathbf{M}_\alpha(c_R^\alpha)\mathrm{Grad}\,[\overline{\mu}_\alpha] \quad \text{with } \alpha = \mathrm{Li}^+, \mathrm{Li}^+_{\mathrm{int}}, \tag{3.16}$$

where $\mathbf{M}_\alpha(c_R^\alpha) = \mathbb{u}_\alpha \overline{c}_R^\alpha \vartheta_R^\alpha (1 - \vartheta_R^\alpha)\mathbf{1}$ is a positive definite mobility tensor for nonlinear isotropic materials [72], and $\mathbb{u}_\alpha$ is the mobility of the species α, here assumed as a constant in time and space. We eventually get

$$\vec{H}_\alpha = -\mathbb{D}_\alpha \mathrm{Grad}\,[c_R^\alpha] - F\mathbb{u}_\alpha \overline{c}_R^\alpha \vartheta_R^\alpha (1 - \vartheta_R^\alpha)\mathrm{Grad}\,[\phi], \tag{3.17}$$

where $\mathbb{D}_\alpha = \mathrm{RT}\mathbb{u}_\alpha$ is the species diffusivity [71].

(b) Cathode

We consider henceforth electrodes with porous microstructures and active particles of intercalation type, such as $\mathrm{LiCoO_2}$. During intercalation, lithium maintains its ionic nature [18] but ions are 'shielded' by their own electrons and, from a macroscopic point of view, the intercalating lithium can be modelled as a neutral species. For this sake, we adopt the symbol $\mathrm{Li}^{\oplus}$ to refer to Li in the cathode in contrast to the notation Li^+ adopted in the electrolyte [73]. Note that the present formulation focuses on the scale of the active material particles, treated as a continuum solid phase. Unlike homogenized macroscopic frameworks, such as the P2D model [74], which accounts for the simultaneous contribution of electronic transport in the solid matrix and ionic transport in the electrolyte pores, the current framework describes the internal dynamics as the diffusion of a neutral intercalated species. This is consistent with the fact that lithium ions are effectively shielded by their corresponding electrons upon entering the lattice, maintaining local charge neutrality.

The mass balance equation for $\mathrm{Li}^{\oplus}$ species reads

$$\frac{\partial}{\partial t} c_R^{\mathrm{Li}^{\oplus}} + \mathrm{Div}[\vec{H}_{\mathrm{Li}^{\oplus}}] = 0. \tag{3.18}$$

Assuming the state variables[11] to be $T, c_{\mathrm{R}}^{\mathrm{Li}^{\oplus}}, \boldsymbol{C}$, the Clausius–Duhem inequality in equation (2.11), under the assumption of thermal equilibrium, reads

$$\left(\mu_{\mathrm{Li}^{\oplus}} - \frac{\partial \psi_{\mathrm{R}}}{\partial c_R^{\mathrm{Li}^{\oplus}}}\right) \frac{\partial c_R^{\mathrm{Li}^{\oplus}}}{\partial t} - \left(\frac{\partial \psi_{\mathrm{R}}}{\partial T} + \eta_{\mathrm{R}}\right) \frac{\partial T}{\partial t} + \left(\frac{\boldsymbol{S}}{2} - \frac{\partial \psi_{\mathrm{R}}}{\partial \boldsymbol{C}}\right) \cdot \frac{\partial \boldsymbol{C}}{\partial t} - \vec{H}_{\mathrm{Li}^{\oplus}} \cdot \mathrm{Grad}\,[\mu_{\mathrm{Li}^{\oplus}}] \geq 0. \tag{3.19}$$

Applying the Coleman–Noll procedure, the constitutive prescriptions equation (2.12) are specified as

$$\eta_{\mathrm{R}} = -\frac{\partial \psi_{\mathrm{R}}}{\partial T}, \quad \boldsymbol{S} = 2\frac{\partial \psi_{\mathrm{R}}}{\partial \boldsymbol{C}}, \quad \mu_{\mathrm{Li}^{\oplus}} = \frac{\partial \psi_{\mathrm{R}}}{\partial c_{\mathrm{R}}^{\mathrm{Li}^{\oplus}}}. \tag{3.20}$$

The constraint

$$\vec{H}_{\mathrm{Li}^{\oplus}} \cdot \mathrm{Grad}\,[\mu_{\mathrm{Li}^{\oplus}}] \leq 0, \tag{3.21}$$

depicts the dissipative contributions.

Experimental evidence [75] shows that cathodic host materials suffer from volumetric swelling upon ionic intercalation and removal. Being generally brittle, active particles provide a purely elastic response if the swelling is constrained. Limiting our investigation to isothermal and adiabatic processes, the (isotropic) swelling is captured by the multiplicative decomposition $\boldsymbol{F} = \boldsymbol{F}^e \boldsymbol{F}^s$, a restriction of equation (2.3). The following identities emerge:

$$\boldsymbol{C} = J_s^{2/3} \boldsymbol{C}^e, \quad \boldsymbol{C}^e = \boldsymbol{F}^{eT} \boldsymbol{F}^e, \quad 2\boldsymbol{E}^e = \boldsymbol{C}^e - \boldsymbol{1}, \quad \boldsymbol{C}^s = J_s^{2/3} \boldsymbol{1}, \quad J_s = 1 + \omega_{\mathrm{Li}^{\oplus}} \left(c_{\mathrm{R}}^{\mathrm{Li}^{\oplus}} - c_{\mathrm{R}}^{\mathrm{Li}_0^{\oplus}}\right), \tag{3.22}$$

with $\omega_{\mathrm{Li}^{\oplus}}$ being the chemical expansion coefficient, and $c_{\mathrm{R}}^{\mathrm{Li}_0^{\oplus}}$ the concentration of $\mathrm{Li}^{\oplus}$ that corresponds to the pristine state [48].

The Helmholtz free energy decomposition equation (2.16) relates to porous cathodes by neglecting the electromagnetic and the inelastic contributions. Denoting with $\bar{c}_{\mathrm{R}}^{\mathrm{Li}^{\oplus}}$ the saturation concentration [56] of ionic species in the hosting material and $\theta_{\mathrm{R}}^{\mathrm{Li}^{\oplus}} = c_{\mathrm{R}}^{\mathrm{Li}^{\oplus}} / \bar{c}_{\mathrm{R}}^{\mathrm{Li}^{\oplus}}$, it reads

$$\psi_{\mathrm{R}} = \underbrace{\mu_0^{\alpha} c_{\mathrm{R}}^{\mathrm{Li}^{\oplus}}}_{\psi_{\mathrm{R}}^0} + \underbrace{\mathrm{RT}\, \bar{c}_{\mathrm{R}}^{\mathrm{Li}^{\oplus}} \left[\theta_{\mathrm{R}}^{\mathrm{Li}^{\oplus}} \ln \theta_{\mathrm{R}}^{\mathrm{Li}^{\oplus}} + \left(1 - \theta_{\mathrm{R}}^{\mathrm{Li}^{\oplus}}\right) \ln\left(1 - \theta_{\mathrm{R}}^{\mathrm{Li}^{\oplus}}\right) + \chi\, \theta_{\mathrm{R}}^{\mathrm{Li}^{\oplus}} \left(1 - \theta_{\mathrm{R}}^{\mathrm{Li}^{\oplus}}\right)\right]}_{\psi_{\mathrm{R}}^{\mathrm{mix}}} + \underbrace{J_s \psi^{\mathrm{el}}}_{\psi_{\mathrm{R}}^{\mathrm{mec}}}. \tag{3.23}$$

Although intercalation electrodes do not show prominent phase segregation, the interaction energy has been accounted for in the energy of mixing $\psi_{\mathrm{R}}^{\mathrm{mix}}$. The elastic energy $\psi_{\mathrm{R}}^{\mathrm{mec}}$ is defined in the intermediate configuration,

$$\psi^{\mathrm{el}} = \mathrm{G}\left(c_{\mathrm{R}}^{\mathrm{Li}^{\oplus}}\right) \boldsymbol{E}^e \cdot \boldsymbol{E}^e + \frac{\lambda\left(c_{\mathrm{R}}^{\mathrm{Li}^{\oplus}}\right)}{2} \mathrm{tr}[\boldsymbol{E}^e]^2,$$

and pulled back in the reference one. Material parameters G, λ, K depend upon $c_{\mathrm{R}}^{\mathrm{Li}^{\oplus}}$ although, for the sake of readability, it will not be written explicitly in the rest of the section.

---

[11] See the electronic supplementary material—*§3: Thermodynamics for a Larché–Cahn system*—for in-depth discussions.

In view of the selection equation (3.23) of the Helmholtz free energy, simple algebra leads to the constitutive equations

$$\boldsymbol{S} = J_s^{-1/3}\left[G\boldsymbol{C} + \frac{\lambda}{2}\mathrm{tr}[\boldsymbol{C}]\mathbf{1} - \frac{3}{2}KJ_s^{2/3}\mathbf{1}\right] \tag{3.24}$$

and

$$\mu_{\mathrm{Li}^\oplus} = \mu_0^{\mathrm{Li}^\oplus} + \mathrm{RT}\left[\ln\left(\frac{\theta_{\mathrm{R}}^{\mathrm{Li}^\oplus}}{1-\theta_{\mathrm{R}}^{\mathrm{Li}^\oplus}}\right) + \chi\left(1 - 2\theta_{\mathrm{R}}^{\mathrm{Li}^\oplus}\right)\right] + \omega_{\mathrm{Li}^\oplus}\mathsf{f}^{ca}_{Li^\oplus}\left(c_R^{\mathrm{Li}^\oplus}, \boldsymbol{C}\right), \tag{3.25}$$

where

$$\begin{aligned}\mathsf{f}^{ca}_{\mathrm{Li}^\oplus}(c_R^{\mathrm{Li}^\oplus}, \boldsymbol{C}) &= \psi^{\mathrm{el}} - \frac{J_s^{-4/3}}{3}\left[G\boldsymbol{C}\cdot\boldsymbol{C} + \frac{\lambda}{2}\mathrm{tr}[\boldsymbol{C}]^2 - \frac{3}{2}K\mathrm{tr}[\boldsymbol{C}]J_s^{2/3}\right]\\ &\quad + \frac{J_s}{\omega_{\mathrm{Li}^\oplus}}\left(\frac{\partial G}{\partial c_{\mathrm{R}}^{\mathrm{Li}^\oplus}}\boldsymbol{E}^e\cdot\boldsymbol{E}^e + \frac{1}{2}\frac{\partial\lambda}{\partial c_{\mathrm{R}}^{\mathrm{Li}^\oplus}}\mathrm{tr}[\boldsymbol{E}^e]^2\right)\\ &= \psi^{\mathrm{el}} - \frac{1}{3J_s}\mathrm{tr}[\boldsymbol{S}\boldsymbol{C}] + \frac{J_s}{\omega_{\mathrm{Li}^\oplus}}\left(\frac{\partial G}{\partial c_{\mathrm{R}}^{\mathrm{Li}^\oplus}}\boldsymbol{E}^e\cdot\boldsymbol{E}^e + \frac{1}{2}\frac{\partial\lambda}{\partial c_{\mathrm{R}}^{\mathrm{Li}^\oplus}}\mathrm{tr}[\boldsymbol{E}^e]^2\right).\end{aligned}$$

To comply with the constitutive constraint given by the Clausius–Duhem inequality equation (3.21), the following Fickian type law is adopted [46,69,71]:

$$\vec{H}_{\mathrm{Li}^\oplus} = -\mathbf{M}_{\mathrm{Li}^\oplus}(c_R^{\mathrm{Li}^\oplus})\,\mathrm{Grad}\,[\mu_{\mathrm{Li}^\oplus}], \tag{3.26}$$

where $\mathbf{M}_{\mathrm{Li}^\oplus}(c_R^{\mathrm{Li}^\oplus}) = \text{ɥ}_{\mathrm{Li}^\oplus}\bar{c}_R^{\mathrm{Li}^\oplus}\,\theta_R^{\mathrm{Li}^\oplus}(1-\theta_R^{\mathrm{Li}^\oplus})\mathbf{1}$ is the positive definite mobility tensor for nonlinear isotropic materials [46,71,72] and

$$\mathrm{Grad}\,[\mu_{\mathrm{Li}^\oplus}] = \frac{\partial^2\psi_{\mathrm{R}}}{\partial c_{\mathrm{Li}^\oplus}^2}\mathrm{Grad}\,[c_{\mathrm{Li}^\oplus}] + \frac{\partial^2\psi_{\mathrm{R}}}{\partial c_{\mathrm{Li}^\oplus}\partial\boldsymbol{C}}\cdot\mathrm{Grad}\,[\boldsymbol{C}].$$

Finally, an *ohmic type law* has been selected to model the flux of electrons in the active particles and the lithium metal anode,

$$\vec{I} = -k_R^{\phi}\mathrm{Grad}\,[\phi], \tag{3.27}$$

with k_R^{ϕ} the electrical conductivity.

(c) Lithium anode

Since the melting temperature of lithium is $T_m = 453.5\,\mathrm{K}$, lithium deforms viscoplastically [38,39], rather than rate-independently, at room temperature $T = 298\,\mathrm{K}$. Assuming that the Helmholtz free energy per unit referential volume is defined by the state variables T and $\boldsymbol{C}^e$, the Clausius–Duhem inequality equation (2.11) becomes[12]

$$-\left(\frac{\partial\psi_{\mathrm{R}}}{\partial T} + \eta_{\mathrm{R}}\right)\frac{\partial T}{\partial t} + \left(\frac{\boldsymbol{S}^e}{2} - \frac{\partial\psi_{\mathrm{R}}}{\partial\boldsymbol{C}^e}\right)\cdot\frac{\partial\boldsymbol{C}^e}{\partial t} + \boldsymbol{M}^e\cdot\boldsymbol{l}^p \geq 0 \tag{3.28}$$

in the assumption of thermal equilibrium. As usual, the plastic flow is assumed to be isochoric, i.e. $J^p = \det(\boldsymbol{F}^p) = 1$. The Coleman–Noll procedure yields the following functional forms for the

---

[12] See the electronic supplementary material—§3: *Thermodynamics for a Larché–Cahn system*—for in-depth discussions.

constitutive relations:

$$\eta_{\mathrm{R}} = -\frac{\partial \psi_{\mathrm{R}}}{\partial T} \quad \text{and} \quad \boldsymbol{S}^e = 2\frac{\partial \psi_{\mathrm{R}}}{\partial \boldsymbol{C}^e}, \tag{3.29}$$

whence

$$\boldsymbol{M}^e \cdot \boldsymbol{l}^p \geq 0. \tag{3.30}$$

As for the solid electrolyte and the cathode, the Helmholtz free energy is of Saint Venant type [76]:

$$\psi_{\mathrm{R}} = \mathrm{G}\boldsymbol{E}^e \cdot \boldsymbol{E}^e + \frac{\lambda}{2}\mathrm{tr}[\boldsymbol{E}^e]^2 \tag{3.31}$$

and the elastic second Piola stresses read

$$\boldsymbol{S}^e = 2G\boldsymbol{E}^e + \lambda\,\mathrm{tr}[\boldsymbol{E}^e]\boldsymbol{1} \quad \text{and} \quad \boldsymbol{S} = \boldsymbol{F}^{p-1}\boldsymbol{S}^e\boldsymbol{F}^{p-T}. \tag{3.32}$$

The viscoplastic behaviour of lithium follows Anand's model [37–39] with slight modifications. It is a single-scalar internal variable formulation (the deformation flow resistance S), with no explicit yield condition and loading/unloading criterion [77]. The evolution equation for the plastic distortion $\boldsymbol{F}^p$:

$$\dot{\boldsymbol{F}}^p = \boldsymbol{D}^p\boldsymbol{F}^p \tag{3.33}$$

is defined by

$$\boldsymbol{D}^p = \frac{3}{2}\frac{\mathrm{dev}[\boldsymbol{S}^e]}{\overline{\sigma}}\bar{\epsilon}^p_v, \tag{3.34}$$

in terms of the equivalent plastic shear strain rate $\bar{\epsilon}^p_v = \sqrt{\frac{2}{3}}||\boldsymbol{D}^p||$ and the von Mises stress

$$\overline{\sigma} = \sqrt{\frac{3}{2}}||\mathrm{dev}[\boldsymbol{S}^e]||.$$

It is assumed that the equivalent plastic shear strain rate depends upon the flow resistance S, which represents the averaged isotropic resistance to plastic flow [77], as listed below:

$$\bar{\epsilon}^p_v = \bar{\epsilon}^p_{v_0}\left(\frac{\overline{\sigma}}{S}\right)^{1/m} \quad \text{and} \quad \dot{S} = \left[H_0\left(1 - \frac{S}{S*}\right)^a\right]\bar{\epsilon}^p_v, \tag{3.35}$$

where $\bar{\epsilon}^p_{v_0}$ is the reference strain rate, $m \in (0, 1]$ is a strain-rate-sensitivity parameter, H_0, a are two strain hardening parameters and S^* denotes a saturation value of S. The evolution equations for $\boldsymbol{F}^p$ and S need to be accompanied by initial conditions. Typical initial conditions presume that at time $t = 0$, $\boldsymbol{F}(\vec{X}, 0) = \boldsymbol{F}^p(\vec{X}, 0) = \boldsymbol{1}$, $S(\vec{X}, 0) = S_0$, so that $\boldsymbol{F}^e(\vec{X}, 0) = \boldsymbol{1}$. In §4, the set of constitutive parameters for lithium foil is provided.

(d) Governing equations

Governing equations emanate from the balance and constitutive equations described for each component of the solid-state cell, equipped with interface, boundary and initial conditions. We defer the description of those conditions to the next section.

4. Numerical simulation of an all-solid-state coin cell battery

Consider the coin cell battery shown in figure 3, consisting of a lithium anode foil with thickness $\mathrm{L}_a = 60\,\mu\mathrm{m}$ a LiPON layer ($\mathrm{L}_e = 60\,\mu\mathrm{m}$) and a positive $\mathrm{LiCoO_2}$ electrode with thickness $\mathrm{L}_c = 18.5\,\mu\mathrm{m}$, deposited on an aluminium collector ($\mathrm{L}_{\mathrm{col}} = 20\,\mu\mathrm{m}$). The cell has a diameter of 2 mm, resulting in a transverse surface area of $A = 3.1416\,\mathrm{mm}^2$. The cathodic volume is therefore

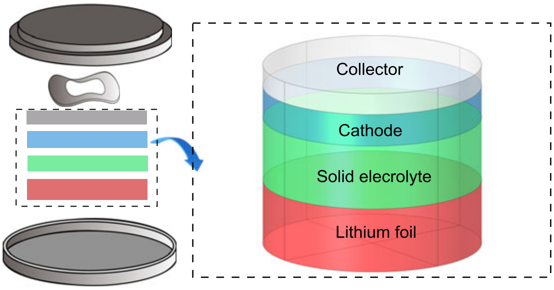

Figure 3. Schematic representation of the all-solid-state electrochemical cell used to validate the proposed model.

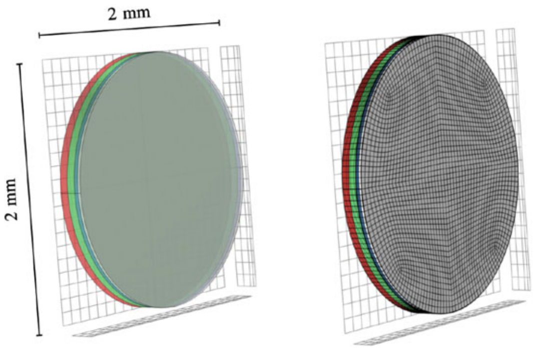

Figure 4. 3D mesh for the numerical simulations, consisting of 23 800 volume elements with quadratic Lagrangian shape functions.

$V_{ca} = 18.5\pi \times 10^{-12}\,\mathrm{m}^3$, whence the maximum amount of lithium that can be stored in the cathode is

$$V_{ca} \times \bar{c}_{\mathrm{R}}^{\mathrm{Li}^{\oplus}} = 1.395 \times 10^{-6}\,\mathrm{mol}. \tag{4.1}$$

Since the amount of lithium in the anode,

$$V_{an} \times c_{\mathrm{R}}^{\mathrm{Li}} = 60\pi \times 10^{-12}\,\mathrm{m}^3 \times 77500\,\mathrm{mol\,m}^{-3} = 1.46 \times 10^{-5}\,\mathrm{mol}, \tag{4.2}$$

is much higher, the capacity of the battery can be estimated from the amount of lithium that can be stored in the cathode, considering that at full charge no more than half of the lithium in a $LiCoO_2$ electrode will be extracted. The capacity of the battery is estimated as

$$0.5 \times F \times V_{ca} \times \bar{c}_{\mathrm{R}}^{\mathrm{Li}^{\oplus}} = 0.067\mathrm{C} = 1.869 \times 10^{-5}\,\mathrm{A\,h}. \tag{4.3}$$

A galvanostatic discharge process is simulated. The electric potential is set to zero at the outer side of the anode, corresponding to $Z = 0$ in figure 5. At full charge state, the open cell voltage is 4.2 V. The imposed current density I_{bat} is applied as a Neumann boundary condition at the top of the cell:

$$\vec{I}(X, Y, Z = L_{\mathrm{B}}, t) \cdot \vec{N} = -I_{\mathrm{bat}}, \tag{4.4}$$

and kept constant in time after a brief smooth transient regime. Symbol $\vec{N}$ in equation (4.4) denotes the outward normal to the corresponding surface. Different current densities are applied to the cell, ranging from $I_{\mathrm{bat}} = 1\,\mathrm{A\,m}^{-2}$ to $I_{\mathrm{bat}} = 2.5\,\mathrm{A\,m}^{-2}$ with steps of $0.25\,\mathrm{A\,m}^{-2}$. Since the current density corresponding to a unit C-rate is $I_1 = 5.85\,\mathrm{A\,m}^{-2}$, the applied C-rates range from 0.168 to 0.420 with steps of 0.042.

The numerical approximation of the governing equations has been carried out using the COMSOL Multiphysics finite-element software, through the 'PDE Interface' module which

Table 1. Model parameters for an all-solid-state electrochemical cell used in the numerical simulations. Different colours are used to indicate the properties of the individual components: red for the anode, green for the electrolyte, cyan for the cathode, and grey for the collector.

input parameters			
parameter	value	unit	description
T	298.5	K	temperature
L_a	60×10^{-6}	m	anode thickness
L_e	60×10^{-6}	m	electrolyte thickness
L_c	18.5×10^{-6}	m	cathode thickness
L_{co}	20×10^{-6}	m	collector thickness
L_{B}	158.5×10^{-6}	m	battery thickness
A	3.14×10^{-6}	m^2	transversal surface area
$\bar{c}_{\mathrm{R}}^{\mathrm{Li}^{\oplus}}$	2.40×10^{4}	$\mathrm{mol\ m^{-3}}$	maximum concentration of $\mathrm{Li}^{\oplus}$ ions in the electrode
k_{an}	1.1×10^{7}	$\mathrm{S\ m^{-1}}$	electrical conductivity in the lithium anode
k_{ca}	1.0×10^{6}	$\mathrm{S\ m^{-1}}$	electrical conductivity in the cathode [78]
k_{col}	3.77×10^{7}	$\mathrm{S\ m^{-1}}$	electrical conductivity in the cathodic collector (aluminium)
k_f^1	1.125×10^{-5}	$\mathrm{s^{-1}}$	lithium ion generation reaction rate constant for equation 1
k_b^1	0.90×10^{-8}	$\mathrm{m^3/(mol\ s)}$	lithium ion recombination reaction rate constant for equation 1
k_f^2	8.10×10^{-9}	$\mathrm{s^{-1}}$	lithium ion generation reaction rate constant for equation 2
k_b^2	0.90×10^{-8}	$\mathrm{m^3/(mol\ s)}$	lithium ion recombination reaction rate constant for equation 2
α_n	0.5	—	charge transfer coefficient for the negative electrode
α_p	0.5	—	charge transfer coefficient for the positive electrode
$\mathbb{D}_{\mathrm{Li}^+}$	5.10×10^{-15}	$\mathrm{m^2\ s^{-1}}$	diffusion coefficient for Li^+ ions in the electrolyte [79]
$\mathbb{D}_{\mathrm{Li}^+_{\mathrm{int}}}$	0.90×10^{-15}	$\mathrm{m^2\ s^{-1}}$	diffusion coefficient for $\mathrm{Li}^+_{\mathrm{int}}$ ions in the electrolyte [79]
$\mathbb{D}_{\mathrm{Li}^{\oplus}}$	1.80×10^{-15}	$\mathrm{m^2\ s^{-1}}$	diffusion coefficient for $\mathrm{Li}^{\oplus}$ ions in the cathode[79]
k_1	5.10×10^{-6}	$\mathrm{m^{2.5}\ mol^{-0.5}\ s^{-1}}$	standard reaction rate constant for anodic reaction [79]
k_2	1.09×10^{-5}	$\mathrm{m\ s^{-1}}$	standard reaction rate constant for cathodic reaction [18]
$\varepsilon_{r,el}$	2.25	—	relative permittivity in the solid electrolyte [18]
$\omega_{Li^{\oplus}}$	-2.4×10^{-7}	$\mathrm{m^3\ mol^{-1}}$	chemical expansion coefficient [80]
K_{el}	71.80	GPa	bulk modulus in the solid electrolyte [81]
G_{el}	41	GPa	shear modulus in the solid electrolyte [81]
K_{ca}	129.4	GPa	bulk modulus in the cathode [82]
G_{ca}	80	GPa	shear modulus in the cathode [82]
K_{col}	70.3	GPa	bulk modulus in the collector
G_{col}	26.9	GPa	shear modulus in the collector

allows specifying PDEs in strong form. Figure 4 shows the spatial discretization of the cell using 23 800 volume elements with quadratic Lagrangian shape functions. The time-dependent problem is solved using an implicit numerical technique with time increments of $\Delta t = 1.0\,\mathrm{s}$. While the cell remains in thermal equilibrium at a temperature-controlled condition of 25°C, the $\mathrm{LiCoO_2}$ cathode shrinks upon ionic insertion. In §4b, various geometric configurations of the cathode are examined, highlighting their effect on the electrochemical response of the entire cell.

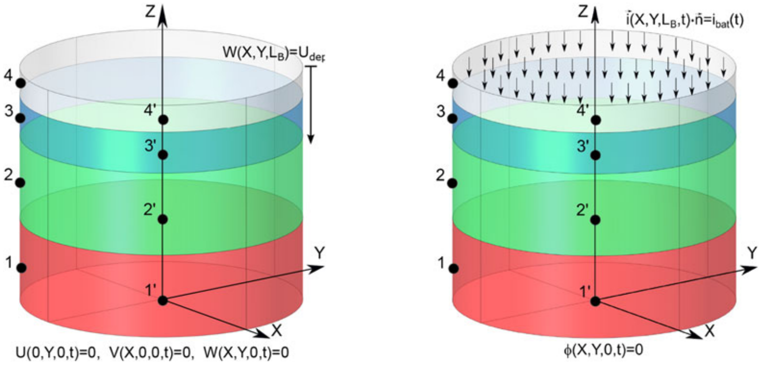

Figure 5. Boundary conditions applied to the cell. (A) *Mechanical boundary conditions*: on the bottom of the cell, the longitudinal displacement is fixed, radial expansion is ensured; on the top, a vertical displacement $\vec{U}_{dep}$ is prescribed. (B) *Electrochemical boundary conditions*: electric potential is set to zero at the free end of the anode, and a density current $I_{\mathrm{bat}}(t)$ is applied at the free ends of the collector.

Table 2. Estimated values of the mechanical parameters for lithium foil anode, from [39].

material parameters of the lithium foil anode			
parameter	value	unit	description
K_{an}	5.95	GPa	bulk modulus in the anode
G_{an}	2.83	GPa	shear modulus in the anode
A	4.25×10^4	s^{-1}	bulk modulus in the anode
Q	37	$\mathrm{kJ\,mol^{-1}}$	activation energy
m	0.15	—	strain-rate-sensitivity parameter
S_0	0.95	MPa	flow resistance ($S(\vec{X},t)$), ($\vec{X}$)
H_0	10	MPa	strain-hardening parameters
S^*	2.00	MPa	saturation value of S.
a	2.0	—	strain-hardening parameters
n	0.05	—	strain-hardening parameters

Mechanical material parameters λ, G and K, which can be made dependent on concentrations as described in §3b, are henceforth taken as constants in time. They are listed in table 1 together with the electrochemical and geometrical parameters used in numerical simulations. The elasto-visco-plastic parameters for the lithium foil, reported in [39], are listed in table 2.

Boundary and initial conditions depicted in figure 5 are listed below. At time $t = 0$, the species concentrations within the electrolyte are uniform, satisfying thermodynamic equilibrium for reactions (3.4), as detailed in full in [18]:

$$\left.\begin{aligned} & c_{\mathrm{R}}^{\mathrm{LiO}}(\vec{\mathrm{X}},0) = 4.93 \times 10^4\,\mathrm{mol\,m^{-3}}, \quad c_{\mathrm{R}}^{\mathrm{n}^-}(\vec{\mathrm{X}},0) = 1.08 \times 10^4\,\mathrm{mol\,m^{-3}} \\ \text{and} \qquad & c_{\mathrm{R}}^{\mathrm{Li}^+}(\vec{\mathrm{X}},0) = 5.68 \times 10^3\,\mathrm{mol\,m^{-3}}, \quad c_{\mathrm{R}}^{\mathrm{Li}^+_{\mathrm{int}}}(\vec{\mathrm{X}},0) = 5.12 \times 10^3\,\mathrm{mol\,m^{-3}}. \end{aligned}\right\} \tag{4.5a}$$

The concentration of lithium in the cathode corresponds to a stoichiometry $\mathrm{Li_{0.5}CoO_2}$, normally adopted at fully charged cells:

$$c_{\mathrm{R}}^{\mathrm{Li}^\oplus}(\vec{\mathrm{X}},0) = c_{\mathrm{R}}^{\mathrm{Li}_0^\oplus} = 0.5 \times \bar{c}_{\mathrm{R}}^{\mathrm{Li}^\oplus}\ \mathrm{mol\,m^{-3}}. \tag{4.5b}$$

The molar density of lithium is $c_{\mathrm{R}}^{\mathrm{Li}}(\vec{\mathrm{X}},0) = 7.69 \times 10^4\,\mathrm{mol\ m^{-3}}$ in the anodic foil.

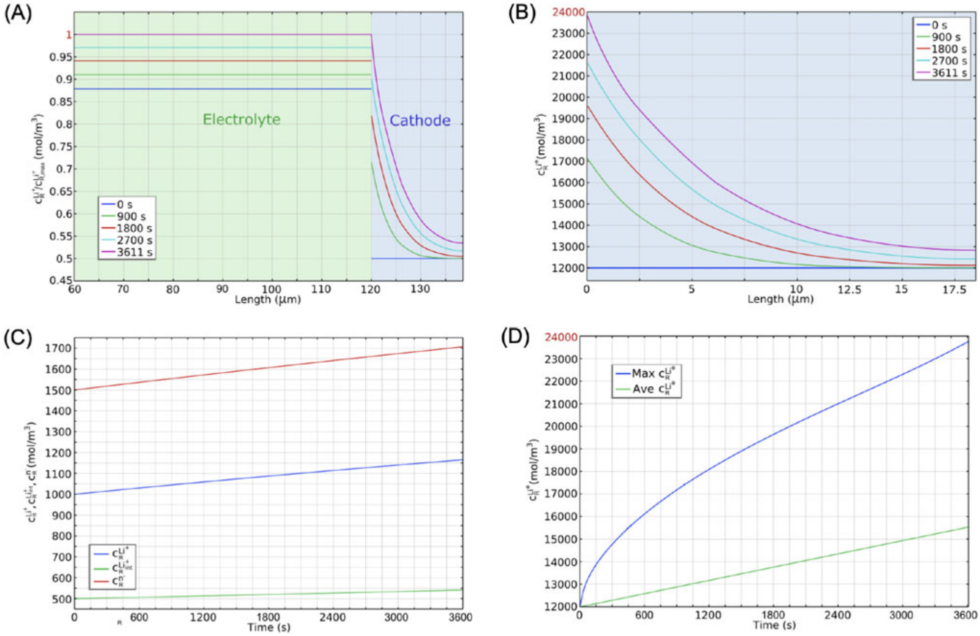

Figure 6. (A) Referential and normalized *lithium concentration* profiles at different time steps. The sum $c_R^{\mathrm{Li}^+} + c_R^{\mathrm{Li}^+_{\mathrm{int}}}$ is plotted in the solid electrolyte. (B) Magnification of the *lithium concentration* profile inside the cathode. (C) Lithium concentration profiles $c_R^{\mathrm{Li}^+}$ (blue line), $c_R^{\mathrm{Li}^+_{\mathrm{int}}}$ (green line), and the uncompensated negative charge $c_R^{\mathrm{n}^-}$ (red line) against time. (D) The maximum concentration (blue line) and average concentration (green line) of lithium inside the cathode against time.

At the electrolyte–electrodes interfaces, the total lithium flux $\vec{H}_{\mathrm{Li}^+_{\mathrm{tot}}}$ is split into two terms, one per each ionic conduction mechanisms described in §3a. The total current is the sum of the two contributions $\vec{I} = F(\vec{H}_{\mathrm{Li}^+} + \vec{H}_{\mathrm{Li}^+_{\mathrm{int}}})$, whereas the hopping H_{Li^+} and interstitial $H_{\mathrm{Li}^+_{\mathrm{int}}}$ fluxes at the electrolyte–electrodes interfaces are derived through interface equations of the Butler–Volmer type, as described in [18].

From the mechanical standpoint, stress-free boundary conditions have been imposed on the lateral surface of the cylindrical coin cell. Dirichlet boundary conditions are applied on the two bases of the cell. At the outer side of the anode, at $Z = 0$, radial displacements are allowed according to the axial-symmetry of the problem. Accordingly, into the COMSOL constraints section, displacements in the Y direction are constrained along the X axis, and vice versa—see figure 5A. On the aluminium current conductor external face, a vertical displacement is uniformly imposed:

$$\vec{U}(X, Y, Z = L_{\mathrm{B}}, t) = -U_{dep}\vec{N}. \tag{4.6}$$

As described in [26,83,84], this approach is taken to replicate the lithium erosion/deposition at the anode/solid electrolyte interface. In particular, during a galvanostatic discharge process, the lithium foil undergoes erosion; this is the reason for the negative sign in equation (4.6). The vertical displacement is the integral in time of the velocity of lithium deposition, i.e.

$$U_{dep} = \int_0^{t_f} \frac{\Omega_{\mathrm{Li}}}{F} I_{bat}\,\mathrm{d}t. \tag{4.7}$$

(a) Planar cathode

In view of the planar shape of the cathode and of the imposed boundary conditions, the electrochemical response of the cell is 1D and the time evolution of the state variables can be plotted as a function of the position X along the cell thickness. Figure 6A,B illustrate the lithium concentration $c_R^{\mathrm{Li}^+}(X)$ at four instants in time, consistent with a current density $I_{\mathrm{bat}} = 1.75\ \mathrm{A\ m^{-2}}$, see the black curve in figure 7. In particular, figure 6A shows the lithium concentration profile, at four different instants, in both electrolyte and cathode (see also magnifications in figure 6B); the curves are normalized with respect to the final concentration value and the saturation limit, respectively. Focusing on the solid electrolyte: the species c_R^{LiO} is consumed, while the concentration of $c_R^{\mathrm{Li}^+}$ rises throughout the discharge process as a result of the ionisation reaction equation (3.1). According to the reaction equation (3.2), the hopping ions indicated by Li^+ grow even if a portion of them is changed into interstitial ions $\mathrm{Li}_{\mathrm{int}}^+$, which also increase. The spatial profiles are uniform,[13] and to provide details, figure 6C shows how these concentrations evolve over time. According to [85], transport dynamics within the electrolytes can exhibit different[13] features depending on whether the system is characterized by anionic mobility or immobilized anions. In the former class, systems are prone to significant concentration polarization and lithium depletion at the electrode–electrolyte interface. Conversely, when anions are immobilized, these phenomena are effectively eliminated, as the fixed anions framework forces lithium transport to proceed almost exclusively via migration. LiPON exhibits a transport behaviour analogous to this second class of systems, although experimental evidence [20,86] reveals a more complex cationic transport mechanism, i.e. a dual-pathway involving both interstitial and hopping motion. Despite this complexity, the immobility of the anionic framework and the requirement for electroneutrality (governed by Maxwell's equations) constrain both Li^+ and $\mathrm{Li}_{\mathrm{int}}^+$ to behave like cations in a single-ion conductor. Consequently, the lithium-ion distribution remains nearly uniform across the electrolyte. Furthermore, in the absence of a concentration gradient to drive ionic motion, these models effectively reduce to Ohm's law [20]. As a consequence, the proposed dual-mechanism model is not merely a numerical exercise, but a necessary framework to account for the stoichiometric evolution of the electrolyte. Specifically, it allows one to track how the consumption of the lithium bound to the non-bridging oxygen atoms (LiO) affects the ratio of mobile species, a feature that provides a more robust physical grounding compared to standard single-mechanism models. Different profiles can be derived by assuming that the reaction rate constants in equation (3.4b) are functions of the electric potential, as in [18]. The electric potential drops almost vertically (see figure 7) when the concentration of lithium $\mathrm{Li}^{\oplus}$ in the cathode approaches its saturation limit $\bar{c}_R^{\mathrm{Li}^{\oplus}} = 24\,000\ \mathrm{mol\ m^{-3}}$ in a narrow region of the cathode close to the electrolyte interface. Cathodic saturation is one of the limiting factors for battery operation: as can be seen from figure 6B, the low ionic diffusivity in the active material causes strong gradients of concentration, which saturate quickly near the interface between electrolyte and cathode if the current is high. The maximum and average concentrations versus time is plotted in figure 6D; the figure highlights that the cathode is far from being saturated when the potential drops to zero, i.e. the discharge process is quite rapid and inefficient as listed in table 3. Intriguingly, although the ratio between intercalated charge (IC) and the theoretical capacity does not surpass the 50%, the one related to the 'nominal' capacity[14] achieved 66%. The latter has been computed by applying a density current equal to $I_{\mathrm{bat}} = 0.2\ \mathrm{A\ m^{-2}}$, see the dash blue line in figure 7B, which corresponds to a C-rate = 0.034. For a detailed discussion on limiting factors in electrochemical cells induced by materials and architectures, see [29].

The norm of the displacement field $||\vec{U}||$ for a density current $I_{\mathrm{bat}} = 1.75\ \mathrm{A\ m^{-2}}$ is plotted in the current configuration in figure 8. The displacement within the cell results from the competition between deposition, here replicated via the imposed displacement at the top of the collector, the cathode swelling upon intercalation and the compliance of the lithium foil. Because of its mechanical weakness, the anode exhibits a remarkable lateral displacement, on the order of 7 µm.

The amplitude of the vertical displacement is shown in figure 9. It highlights that most of the axial deformation occurs in the lithium foil, whereas the electrolyte essentially undergoes a rigid

---

[13] See the electronic supplementary material—Insights into the numerical simulations—for further insights on the topics.

[14] The nominal capacity of the battery is deduced by charging with a current that allows one to charge the battery over a period of 15 or 20 h; this is a value that approximates the theoretical capacity but takes into account the losses and efficiency of the charge/discharge process.

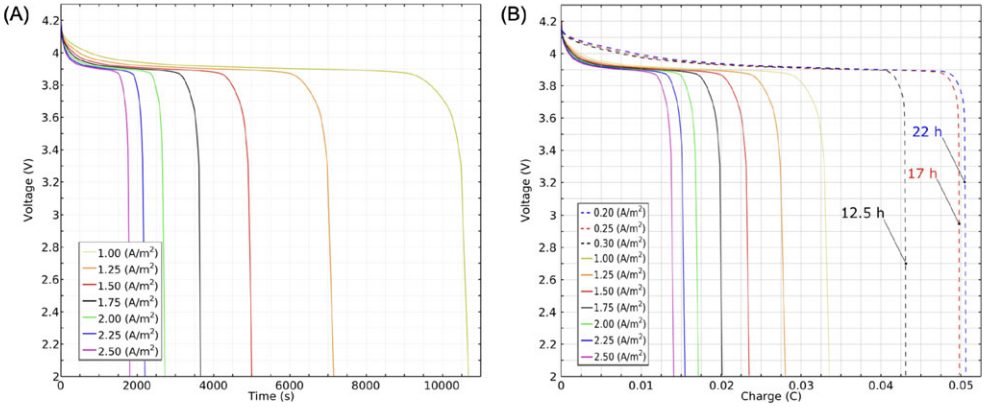

Figure 7. Discharge curves for various density currents ranging from $I_{\mathrm{bat}} = 1\ \mathrm{A\ m^{-2}}$ to $I_{\mathrm{bat}} = 2.50\ \mathrm{A\ m^{-2}}$ as a function of time on the left (A), and as a function of charge on the right (B), in a galvanostatic process.

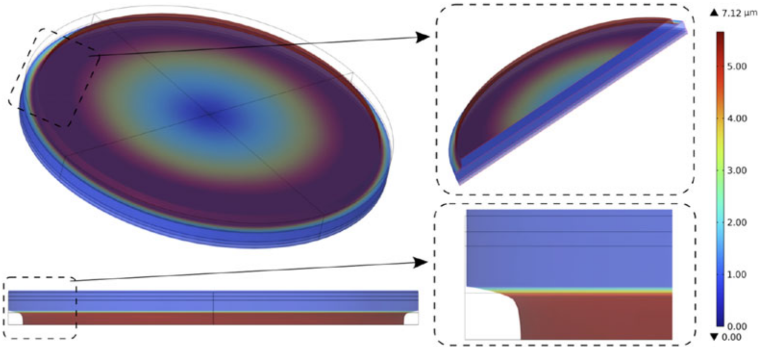

Figure 8. The amplitude of the displacement field $||\vec{U}|| = \sqrt{U^2 + V^2 + W^2}$ within the cell for a density current of $|i_{\mathrm{bat}}| = 1.75\ \mathrm{A\ m^{-2}}$; magnification of the left-hand side of the cell is provided to emphasize the displacement.

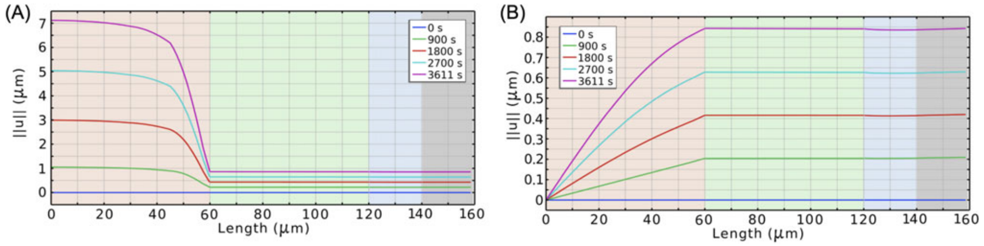

Figure 9. (A) The amplitude of $||\vec{U}||$ along a cut line in the cell centre, at different time steps. (B) The amplitude of $||\vec{U}||$ along a cut line on the lateral cell border, at different time steps.

body motion. The visco-plastic nature of the lithium foil is attested to by the nonlinear response within the anode. In figure 9B, the displacement amplitude is shown along a vertical line on the cell's exterior boundary. Lateral contraction/expansion is permitted, resulting in a significant radial displacement. Because of the confinement of the neighbouring material, the displacement in the longitudinal axis at the cell centre is smaller in proportion to the border.

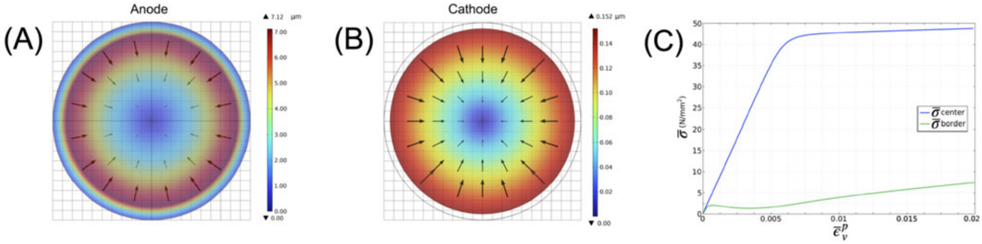

Figure 10. (A) Radial displacement in the anode at the end of the discharge process. The black circle indicates the undeformed configuration. The direction of the black arrows indicates the direction of the displacement. (B) Radial displacement in the cathode when the $\vec{U}_{\text{dep}}$ reaches its highest value at the end of the discharge process, shrinking is induced by lithiation. (C) Stress–strain diagram, in terms of equivalent quantities $\overline{\sigma}$ and $\overline{\epsilon}^p_v$, measured in the centre of the lithium foil (blue line) and at the border (green line) during the discharge cycle (points 1 and 1′ in figure 5, respectively).

Table 3. Electrochemical response of the cell. The last two columns depict the ratio between intercalated charge (IC) and theoretical capacity (capacity$_T$ = 0.0673 C) and nominal capacity (capacity$_N$ = 0.05075 C).

I_{bat} (A m^{-2})	C-rate (—)	discharge time (s)	intercalated charge (IC) (C)	IC/capacity$_T$ (%)	IC/capacity$_N$ (%)
1.00	0.168	10675	0.0335	49.78	66.01
1.25	0.210	7150	0.0280	41.61	55.17
1.50	0.252	5000	0.0235	34.92	46.30
1.75	0.294	3615	0.0200125	29.74	39.43
2.00	0.336	2725	0.01725	25.63	33.99
2.25	0.378	2200	0.0155	23.03	30.54
2.50	0.420	1800	0.014125	20.99	27.83

To have a better understanding of the mechanical response of the cell, it is useful to display its radial displacement. A top-view of the displacements of the electrodes is illustrated in figure 10 at the end of the discharge process. Specifically, figure 10A illustrates the visco-plastic lateral contraction of the lithium foil, whereas figure 10B shows the shrinkage resulting from lithiation of the cathode. During discharge, lithium intercalation induces counterintuitive shrinkage of the cathode because of its negative volumetric expansion coefficient.

The evolution of the equivalent von Mises stress inside the cell is reported in figure 10C against its dual ϵ^p_v. The stress along the axis of symmetry is plotted against the deformation with a blue line, whereas the green line depicts the stress on a vertical line on the lateral surface. The *chemical potential* for the mobile lithium within the cathode is ruled by the expression:

$$\mu_{\text{Li}^\oplus} = \underbrace{\mu_0^{\text{Li}^\oplus} + \text{RT}\left[\ln\left(\frac{\theta_{\text{R}}^{\text{Li}^\oplus}}{1-\theta_{\text{R}}^{\text{Li}^\oplus}}\right) + \chi\left(1 - 2\theta_{\text{R}}^{\text{Li}^\oplus}\right)\right]}_{\mu_{\text{Li}^\oplus}^{\text{diff}}} + \underbrace{\omega_{\text{Li}^\oplus}\left[\psi^{\text{el}} - \frac{\text{tr}[\boldsymbol{SC}]}{3J_s}\right]}_{\mu_{\text{Li}^\oplus}^{\text{mec}}},$$

since λ, K, G are assumed to be concentration independent. The $\mu_{\text{Li}^\oplus}^{\text{diff}}$ contribution has an entropic and an energetic term, where the Flory χ parameter has been set to zero. Figure 11 shows that the mechanical contribution $\mu_{\text{Li}^\oplus}^{\text{mec}}$ is orders of magnitude smaller than $\mu_{\text{Li}^\oplus}^{\text{diff}}$.

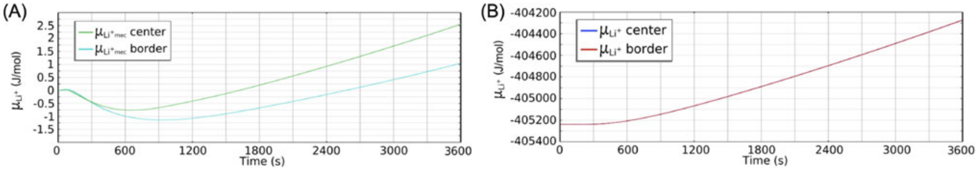

Figure 11. (A) Time evolution of the mechanical contribution at the chemical potential of lithium into the cathode, $\mu_{\mathrm{Li}^\oplus}^{\mathrm{mec}}$, measured both on the centre and on the border of the cathode. (B) Time evolution of the chemical potential of lithium into the cathode, measured both on the centre and on the border of the cathode.

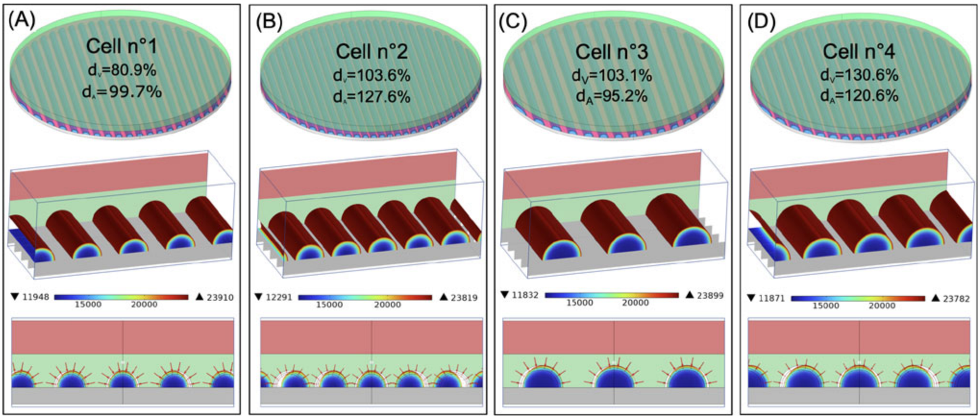

Figure 12. (A–D) Four geometric cell configurations in which parallel bands of semi-cylinder-shaped cathodic material are deposited. The radius of the semi-cylinder and the distance between the bands determine each cathode design. The lithium concentration inside the cathode is reported for each configuration at the bottom and in the middle of the picture. The shrinking of the cathode induced by lithiation is visible at the bottom. The lithium flux at the solid electrolyte/cathode interface is represented by red arrows.

(b) Architected cathodes

Properly designed electrodes enhance electron and ion diffusion, as well as electrolyte penetration into the active materials, by increasing the surface area and maintaining a short ion transport pathway. Architected electrodes offer several advantages over conventional flat-thick electrodes, including greater surface area, shorter ion diffusion paths and improved mechanical strength. These benefits were previously demonstrated through 2D simulations under small strain conditions in [29]. In this work, we extend those investigations to three dimensions, simulating the effects and optimization of 3D-printed lithium iron phosphate ($\mathrm{LiFePO_4}$) electrodes. The geometries studied were experimentally analysed in [41] and are illustrated in figure 12. The latter were inspired by the configurations presented in fig. 2 of [41].

To replicate the 3D-printed geometry of the composite electrodes shown in fig. 2 of [41], we modelled the cathode as an array of semi-cylinders aligned parallel, as illustrated in figure 12. This design approach allowed us to capture the essential structural features of the printed architecture. Based on the cylinder radius R_c and the spacing between adjacent cylinders, four distinct geometric configurations were considered. The corresponding cathode volume and the solid electrolyte–cathode interfacial area (E/C) for each configuration are listed in table 4.

Insights into the performance of each architecture can be derived from two indicators (see table 4): the ratio $\delta_V = V_i/V_0$ of the volume of each cell V_i to the volume of the cell with planar geometry V_0, and the ratio $\delta_A = A_i/A_0$ between the interface E/C A_i of each cell and that of the cell with planar shape A_0. The first parameter quantifies the reduction in cathodic material in

Table 4. Cathode volume and surface of the solid electrolyte/cathode interface, for the four geometric configurations examined and for the reference planar design (cell no. 0).

case study	E/C interface A_i (m^2)	cathode volume V_i (m^3)	$\delta_V = V_i/V_0$	$\delta_A = A_i/A_0$
planar cell no. 0	3.141×10^{-6}	5.812×10^{-11}	—	—
cell no. 1 ($R_c = 30$ µm)	3.132×10^{-6}	4.693×10^{-11}	80.9%	99.7%
cell no. 2 ($R_c = 30$ µm)	4.010×10^{-6}	6.009×10^{-11}	103.6%	127.6%
cell no. 3 ($R_c = 40$ µm)	2.992×10^{-6}	5.978×10^{-11}	103.14%	95.2%
cell no. 4 ($R_c = 40$ µm)	3.789×10^{-6}	7.574×10^{-11}	130.6%	120.6%

Table 5. Time required to discharge the cell and charge extracted at the end of the process, for each set-ups studied and for the reference planar design (cell no. 0). The green cell denotes the design with the best performance in terms of cell efficiency; the red cell represents the worst case.

case study	discharge time (s)	extracted charge (C)	extracted charge density (C/m^3)
planar cell no. 0	3615	0.0200125	0.344
cell no. 1 ($R_c = 30$ µm)	3015	0.016375	0.348
cell no. 2 ($R_c = 30$ µm)	4635	0.0255625	0.427
cell no. 3 ($R_c = 40$ µm)	2895	0.015625	0.261
cell no. 4 ($R_c = 40$ µm)	4440	0.0245	0.323

comparison to a planar design, while the second evaluates the increase or decrease in the contact surface between the electrolyte and the cathode. Four different cells, relative to the planar cell (no. 0), have been designed: cell no. 1, with a δ_A almost equal to that of cell no. 0; cells nos. 2–3, with nearly the same δ_V as cell no. 0; and the final cell, no. 4, with both greater δ_A and δ_V. Specifically, cells no. 2 and no. 3 serve as a comparison with cell no. 0, having the same volume, whereas cells no. 1 and no. 4 allow for further speculation on battery performance.

In the next paragraphs, we examine the response of each cell in terms of extracted charge, to obtain qualitative guidance for the optimal project selection. A current density equal to $i_{\mathrm{bat}} = 1.75\,\mathrm{A\ m^{-2}}$ is applied in all case.

For each cell arrangement in figure 12, the lithium concentration in the cathode is displayed in the centre and at the bottom of each subfigure; a magnification of a representative volume extracted from the cell's centre is shown. Owing to the low ionic diffusivity, it is evident that the lithium concentration increases in a thin layer near the interfaces. The final time step is listed in table 5, when the saturation concentration of lithium is reached. At the bottom of each subfigure, the shrinking of the cathode induced by lithiation is visible. The red arrows indicate the flux of lithium, $\vec{H}_{\mathrm{Li}^+} + \vec{H}_{\mathrm{Li}^+_{\mathrm{int}}}$, highlighting the direction of the flux at the electrolyte/cathode interface.

The discharge curves for the four set-ups are displayed against time in figure 13A. For the sake of comparison, the discharge curve of the cell with a perfectly flat cathode is shown in a dashed line. As the voltage of the cell decreases from its maximum value of 4.2 to 2.0 V, a voltage drop becomes evident when the saturation concentration of the lithium in the cathode $\bar{c}_R^{\mathrm{Li}^\oplus} = 24\,000\,\mathrm{mol\ m^{-3}}$ (the limiting factor) is approached. For each case study, table 5 lists the time required to discharge the cell as well as the charge extracted at the end of the process. To evaluate the efficiency of the cells and compare individual cases, the extracted charge density is shown in the column on the right-hand side, derived by dividing the extracted charge by the volume of cathode material listed in table 4, which corresponds to the cell storage capacity for that specific applied current value $i_{\mathrm{bat}} = 1.75\,\mathrm{A\ m^{-2}}$. Analysing figures 13–14, we can deduce that cell

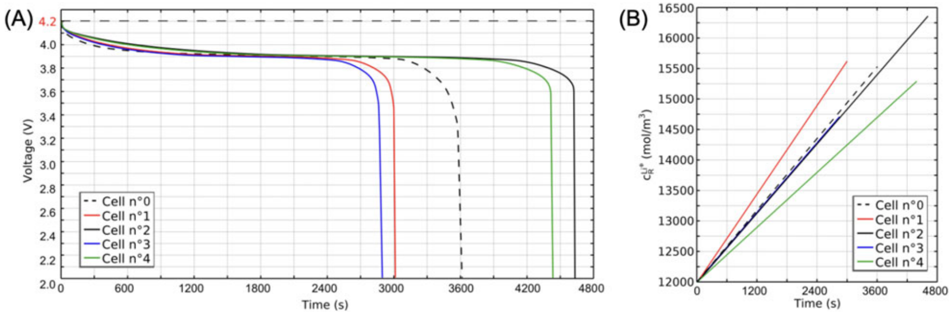

Figure 13. (A) Discharge curves for each of the four set-ups as a function of time. (B) For each of the four designs, the average concentration of lithium inside the cathode.

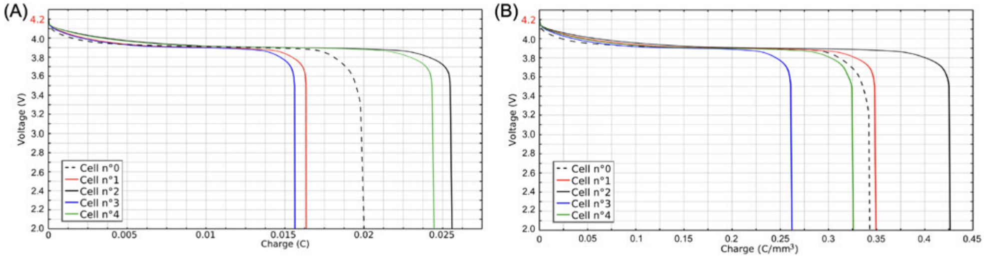

Figure 14. Discharge curves for each of the four set-ups as a function of charge, (A) and a function of charge density, (B).

no. 2 (black line) provides the best configuration, while cell no. 3 (blue line) shows the worst. In fact, for the same volume, architecture number 2 (3) provides a long (short) discharge time and high (low) amounts of IC (figure 14A) and charge density (figure 14B), as also listed in table 5. This is further confirmed by figure 14B, where the evolution of the average concentration in the cathode over time is depicted. Again, we observe that cell no. 2 performs the best. We conclude that, for the same volume, the architecture with a larger interface surface between E/C delivers the most benefits and makes better use of the battery resources.

To explore further, we compare cell no. 0 with cell no. 1, which has the same E/C interface surface. Under this condition, we observe that the cell with less cathodic volume makes better use of the battery's qualities. In fact, although cell no. 1 shows less IC compared to cell no. 0, it outperforms in terms of both the average lithium concentration inside the cathode and the IC density (see figures 13B–14B).

Finally, we compare cell no. 0 with a cell having higher cathodic volume and E/C interface surface, namely cell no. 4. Interestingly, this new configuration outperforms no. 0 in terms of IC but performs worse in terms of IC density and average lithium concentration inside the cathode. We can conclude that, although the high E/C surface interface allows for a higher IC, excessively increasing the cathode volume is unnecessary, as the saturation limit remains a restricting factor, preventing the full utilization of the active material.

In fact, the average lithium ion concentration inside the cathode is a clear indicator of the level of its utilization. A higher concentration suggests better cathode efficiency, which translates to a larger capacity storage density. Cell no. 2 has the highest concentration and the longest discharge time, which might translate to the maximum efficiency in terms of extracted charge density, as reported by the green cell in table 5. Cell no. 1, although having the shortest time to discharge (lower extracted charge), has higher average concentration values within the cathode than cells no. 3 and no. 4, thus indicating a greater extracted charge density. Excluding the planar reference cell, cell no. 3 has the worst performance in terms of cell efficiency (extracted charge density), as shown in red in table 4.

5. Conclusion

This work presents a comprehensive electro-chemo-mechanical model for all-solid-state batteries (ASSBs), capturing their inherently multiphysics behaviour. The model, grounded in continuum thermodynamics, couples electrochemical and mechanical phenomena–such as cathode swelling, lithium plating/stripping, and changes in ionic conductivity, to cite a few.

In this study, the response of a complete cell—comprising a metallic lithium foil anode, a solid electrolyte (LiPON) accounting for two ionic conduction mechanisms and a porous $LiCoO_2$ cathode—has been thoroughly investigated. Key quantities such as electric potential, lithium concentration profiles, displacements and stress distributions have been analysed.

The problem has been solved numerically using the finite-element method in Multiphysics, employing the PDE Interface module. Numerical simulations yield valuable insights into the electrochemical behaviour of the cell under galvanostatic discharge, as well as predictions of limiting factors during charge and discharge cycles.

A planar configuration (2032-type coin cell) with a flat cathode–electrolyte interface was examined. Analysis of the lithium concentration profile into the solid electrolyte reveals that the species $c_{\mathrm{R}}^{\mathrm{LiO}}$ is progressively consumed within the solid electrolyte, leading to an increase in the concentration of Li^+ ions throughout the discharge process. This increase follows the ionization reaction and the hopping transport of lithium ions. Although a portion of the ions converts into interstitial lithium ($\mathrm{Li}_{\mathrm{int}}^{+}$), their overall concentration continues to rise. The spatial concentration profiles are approximately uniform, though they evolve over time.

Cathodic saturation is identified as a limiting factor in battery performance. Owing to the low ionic diffusivity in the active material, steep concentration gradients develop near the electrolyte/cathode interface. Higher current densities accelerate this saturation, as more lithium ions are driven into the electrode.

Correspondingly, the electric potential exhibits a sharp drop when the lithium concentration in the cathode nears its saturation limit. The model evaluates different C-rates, simulating the virtual battery's performance under varying current flux. Interestingly, the ratio between the IC and the theoretical capacity does not exceed 50%, while the ratio with respect to the nominal capacity reaches 66%.

The mechanical response within the flat cell is driven by the interplay of lithium erosion (here modelled via an imposed displacement on the current collector), cathode shrinking owing to lithium intercalation and the mechanical compliance of the lithium foil. A multiphysics model, formulated within the framework of finite deformations and aimed at describing the phenomena of plating and stripping, will be the subject of future studies. Significant lateral displacement is observed in the anode, primarily owing to its mechanical softness. Most of the axial deformation occurs in the lithium foil, while the solid electrolyte behaves like a rigid body.

The evolution of von Mises stress within the cell has been analysed. Furthermore, the contribution of mechanical stress to the lithium chemical potential in the cathode has been quantified and compared with the corresponding diffusive component. In this case, both the intensity and gradient of the mechanical contribution $\mu_{\mathrm{Li}^+}^{\mathrm{mec}}$ are negligible compared to the total chemical potential μ_{Li^+} and so the $\mu_{\mathrm{Li}^+}^{\mathrm{diff}}$.

A parametric study on cathode geometry was carried out, highlighting the critical balance between cathode volume and electrolyte/cathode interface surface. Two key geometric indicators were used: the volume ratio $\delta_V = V_i/V_0$, and the surface ratio $\delta_A = A_i/A_0$, where V_0 and A_0 refer to the reference planar cell. Four alternative cell architectures were designed: (i) cell no. 1, which shows the same δ_A as the reference flat cell (cell no. 0), (ii) cells no. 2 and no. 3, which exhibit the same δ_V as no. 0 but different δ_A, (iii) cell no. 4, which features an increased δ_A and δ_V with respect to no. 0.

Comparative analysis shows that cell no. 2, with the largest δ_A, offers the best performance, while cell no. 3, with the smallest δ_A, performs the worst. At equal δ_V, the architecture with greater interface area delivers longer discharge time and higher stored charge and charge density. This indicates that, for a fixed cathode volume, increasing the electrolyte/cathode interface area is advantageous for performance and resource utilization.

Further comparisons between cell no. 0 and cell no. 1, which share the same interface area, reveal that the cell with reduced cathode volume performs better. Although cell no. 1 stores slightly less total charge, it surpasses the flat cell in terms of average lithium concentration and charge density within the cathode.

Finally, cell no. 0 was compared with cell no. 4, which has both a larger cathode volume and interface area. While cell no. 4 stores more lithium overall, its average lithium concentration and inserted charge density are lower. This suggests that excessive cathode volume may not be beneficial, as saturation effects still limit the full utilization of active material—despite the advantages conferred by a larger interface area.

Data accessibility. The numerical implementation script supporting the findings of this study has been made publicly available on Zenodo: [87].

The data are provided in the electronic supplementary material [88].

Declaration of AI use. Yes, we have used AI-assisted technologies in creating this article. During the preparation of this work, the authors used the free version of ChatGPT (GPT-3.5, OpenAI) and Google Gemini to assist with English language proofreading of the manuscript. After using these tools, the authors reviewed and edited the content as needed and take full responsibility for the content of the published article.

Authors' contributions. L.C.: conceptualization, data curation, formal analysis, investigation, methodology, project administration, resources, software, supervision, validation, visualization, writing—original draft, writing—review and editing; M.S.: conceptualization, data curation, formal analysis, investigation, methodology, project administration, resources, supervision, validation, visualization, writing—original draft, writing—review and editing; A.S.: conceptualization, funding acquisition, investigation, methodology, project administration, resources, supervision, validation, visualization, writing—review and editing.

All authors gave final approval for publication and agreed to be held accountable for the work performed therein.

Conflict of interest declaration. We declare we have no competing interests.

Funding. This research is funded by: the European Union's Horizon 2020 research and innovation programme HORIZON-EUROHPC project 'dealii-X: an Exascale Framework for Digital Twins of the Human Body' (topic HORIZON-EUROHPC-JU-2023-COE-03-01). Project grant no. 101172493, the Mechanobiology research center at UNIBS (https://www.mechanobiology-unibs.it/) through the support of companies COMSOL and MDE, the Ferriera Valsabbia foundation and Comipont through generous donations to fund studies in the field of Mechanobiology. The work has been carried out as part of INdAM (Istituto Nazionale di Alta Matematica) GNFM activities.

References

1. Olabi A, Abbas Q, Shinde P, Abdelkareem MA. 2023 Rechargeable batteries: technological advancement, challenges, current and emerging applications. *Energy* **266**, 126408. (doi:10.1016/j.energy.2022.126408)
2. Winter M, Brodd R. 2004 What are batteries, fuel cells, and supercapacitors? *Chem. Rev.* **104**, 4245–4270. (doi:10.1021/cr020730k)
3. Serpelloni M, Cabras L, Esmizadeh S, Yildiz E, Bastanfar M, Valizadeh N, Berlato M, Salvadori A. 2024 4.14 - mechanics of batteries. In *Comprehensive Mechanics of Materials (First Edition)* (ed. V Silberschmidt), 1st edn., pp. 335–354. Oxford: Elsevier. (doi:10.1016/B978-0-323-90646-3.00038-1)
4. Mohammed S, Jung J. 2021 A comprehensive state-of-the-art review of wired/wireless charging technologies for battery electric vehicles: classification/common topologies/future research issues. *IEEE Access* **9**, 19572–19585. (doi:10.1109/ACCESS.2021.3055027)
5. Chen Y *et al.* 2021 A review of lithium-ion battery safety concerns: the issues, strategies, and testing standards. *J. Energy Chem.* **59**, 83–99. (doi:10.1016/j.jechem.2020.10.017)
6. Bistri D, Afshar A, Di Leo C. 2021 Modeling the chemo-mechanical behavior of all-solid-state batteries: a review. *Meccanica* **56**, 1523–1554. (doi:10.1007/s11012-020-01209-y)

7. Boaretto N, Garbayo I, Valiyaveettil-SobhanRaj S, Quintela A, Li C, Casas-Cabanas M, Aguesse F. 2021 Lithium solid-state batteries: state-of-the-art and challenges for materials, interfaces and processing. *J. Power Sourc.* **502**, 229919. (doi:10.1016/j.jpowsour.2021.229919)
8. Famprikis T, Canepa P, Dawson J, Islam MS, Masquelier C. 2019 Fundamentals of inorganic solid-state electrolytes for batteries. *Nat. Mater* **18**, 1278–1291. (doi:10.1038/s41563-019-0431-3)
9. Schnell J, Günther T, Knoche T, Vieider C, Köhler L, Just A, Keller M, Passerini S, Reinhart G. 2018 All-solid-state lithium-ion and lithium metal batteries – paving the way to large-scale production. *J. Power Sourc.* **382**, 160–175. (doi:10.1016/j.jpowsour.2018.02.062)
10. Zheng F, Kotobuki M, Song S, Lai M, Lu L. 2018 Review on solid electrolytes for all-solid-state lithium-ion batteries. *J. Power Sourc.* **389**, 198–213. (doi:10.1016/j.jpowsour.2018.04.022)
11. Boz B, Dev T, Salvadori A, Schaefer J. 2021 Electrolyte and electrode designs for enhanced ion transport properties to enable high performance lithium batteries. *J. Electrochem. Soc.* **168**, 090501. (doi:10.1149/1945-7111/ac1cc3)
12. Han X *et al.* 2017 Negating interfacial impedance in garnet-based solid-state Li metal batteries. *Nat. Mater* **16**, 572–579. (doi:10.1038/nmat4821)
13. Esmizadeh S, Cabras L, Serpelloni M, Dev T, Oancea V, Knobbe E, Lachner M, Salvadori A. 2024 A review on modeling of nucleation and growth of Li dendrites in solid electrolytes. *J. Energy Storage* **97**, 112897. (doi:10.1016/j.est.2024.112897)
14. Sharafi A, Meyer HM, Nanda J, Wolfenstine J, Sakamoto J. 2016 Characterizing the Li–$Li_7La_3Zr_2O_{12}$ interface stability and kinetics as a function of temperature and current density. *J. Power Sourc.* **302**, 135–139. (doi:10.1016/j.jpowsour.2015.10.053)
15. Cheng EJ, Sharafi A, Sakamoto J. 2017 Intergranular Li metal propagation through polycrystalline $Li_{6.25}Al_{0.25}La_3Zr_2O_{12}$ ceramic electrolyte. *Electrochim. Acta* **223**, 85–91. (doi:10.1016/j.electacta.2016.12.018)
16. Aguesse F, Manalastas W, Buannic L, Lopez del Amo JM, Singh G, Llordés A, Kilner J. 2017 Investigating the dendritic growth during full cell cycling of garnet electrolyte in direct contact with Li metal. *ACS Appl. Mater. Inter.* **9**, 3808–3816. (doi:10.1021/acsami.6b13925)
17. Aziz SB, Woo TJ, Kadir M, Ahmed HM. 2018 A conceptual review on polymer electrolytes and ion transport models. *JS: AMD* **3**, 1–17. (doi:10.1016/j.jsamd.2018.01.002)
18. Cabras L, Danilov D, Subber W, Oancea V, Salvadori A. 2022 A two-mechanism and multiscale compatible approach for solid state electrolytes of (Li-ion) batteries. *J. Energy Storage* **48**, 103842. (doi:10.1016/j.est.2021.103842)
19. Eckhardt JK, Kremer S, Fuchs T, Minnmann P, Schubert J, Burkhardt S, Elm MT, Klar PJ, Heiliger C, Janek J. 2023 Influence of microstructure on the material properties of LLZO ceramics derived by impedance spectroscopy and brick layer model analysis. *ACS Appl. Mater. Interfaces* **15**, 47 260–47 277. (doi:10.1021/acsami.3c10060)
20. Cabras L, Danilov D, Subber W, Oancea V, Salvadori A. 2022 A two-mechanism and multiscale compatible approach for solid state electrolytes of (Li-ion) batteries. *J. Energy Storage* **48**, 103842. (doi:10.1016/j.est.2021.103842)
21. Julien C, Mauger A, Zaghib K, Groult H. 2014 Comparative Issues of Cathode Materials for Li-Ion Batteries. *Inorg* **2**, 132–154.
22. Etacheri V, Marom R, Elazari R, Salitra G, Aurbach D. 2011 Challenges in the development of advanced Li-ion batteries: a review. *Energy Environ. Sci.* **4**, 3243–3262. (doi:10.1039/c1ee01598b)
23. Lyu Y, Wu X, Wang K, Feng Z, Cheng T, Liu Y, Wang M, Chen R, Xu L, Zhou J. 2021 An overview on the advances of $LiCoO_2$ cathodes for Lithium-Ion batteries. *Adv. Energy Mater* **11**, 2000982. (doi:10.1002/aenm.202000982)
24. Fabre S, Guy-Bouyssou D, Bouillon P, Le Cras F, Delacourt C. 2011 Charge/discharge simulation of an all-solid-state thin-film battery using a one-dimensional model. *J. Electrochem. Soc.* **159**, A104. (doi:10.1149/2.041202jes)
25. Salvadori A, Grazioli D, Geers M. 2015 Governing equations for a two-scale analysis of Li-ion battery cells. *Int. J. Solids Struct.* **59**, 90–109. (doi:10.1016/j.ijsolstr.2015.01.014)
26. Cabras L, Serpelloni M. 2025 Electro-chemo-mechanics of solid state batteries: inelastic response to lithium plating and stripping. *Proc. R. Soc. London A* **481**, 20240230. (doi:10.1098/rspa.2024.0230)
27. Li G, Monroe CW. 2020 Multiscale lithium-battery modeling from materials to cells. *Annu. Rev. Chem. Biomol.* **11**, 277–310. (doi:10.1146/annurev-chembioeng-012120-083016)

28. Zhao K, Pharr M, Wan Q, Wang W, Kaxiras E, Vlassak J, Suo Z. 2012 Concurrent reaction and plasticity during initial lithiation of crystalline silicon in Lithium-ion batteries. *J. Electrochem. Soc.* **159**, A238–A243. (doi:10.1149/2.020203jes)
29. Magri M, Boz B, Cabras L, Salvadori A. 2022 Quantitative investigation of the influence of electrode morphology in the electro-chemo-mechanical response of li-ion batteries. *Electrochim. Acta* **405**, 139778. (doi:10.1016/j.electacta.2021.139778)
30. Zor C, Turrell SJ, Uyanik MS, Afyon S. 2024 Lithium plating and stripping: toward anode-free solid-state batteries. *Adv. Energy Sustainability Res.* **5**, 2300001. (doi:10.1002/aesr.202300001)
31. Kazyak E, Garcia-Mendez R, LePage W, Sharafi A, Davis A, Sanchez A, Chen K, Haslam C, Sakamoto J, Dasgupta N. 2020 Li penetration in ceramic solid electrolytes: operando microscopy analysis of morphology, propagation, and reversibility. *Matter* **2**, 1025–1048. (doi:10.1016/j.matt.2020.02.008)
32. Jeanne-Brou R, Charvin N, de Moor G, Flandin L, Issa S, Bouchet R, Devaux D. 2023 Ionic conductivity of solid polymer electrolytes depending on elongation. *Electrochim. Acta* **469**, 143253. (doi:10.1016/j.electacta.2023.143253)
33. Sarre G, Blanchard P, Broussely M. 2004 Aging of Lithium-ion batteries. *J. Power Sourc.* **127**, 65–71. (doi:10.1016/j.jpowsour.2003.09.008)
34. Fathiannasab H, Kashkooli A, Li T, Zhu L, Chen Z. 2020 Three-dimensional modeling of all-solid-state lithium-ion batteries using synchrotron transmission X-ray microscopy tomography. *J. Electrochem. Soc.* **167**, 100558. (doi:10.1149/1945-7111/ab9380)
35. Fathiannasab H, Zhu L, Chen Z. 2021 Chemo-mechanical modeling of stress evolution in all-solid-state lithium-ion batteries using synchrotron transmission X-ray microscopy tomography. *J. Power Sourc.* **483**, 229028. (doi:10.1016/j.jpowsour.2020.229028)
36. Bielefeld A, Weber D, Janek J. 2019 Microstructural modeling of composite cathodes for all solid state batteries. *J. Phys. Chem. C* **123**, 1626–1634. (doi:10.1021/acs.jpcc.8b11043)
37. Brown SB, Kim KH, Anand L. 1989 An internal variable constitutive model for hot working of metals. *Int. J. Plast.* **5**, 95–130. (doi:10.1016/0749-6419(89)90025-9)
38. Narayan S, Anand L. 2018 A large deformation elastic–viscoplastic model for lithium. *Extreme Mech. Lett.* **24**, 21–29. (doi:10.1016/j.eml.2018.08.006)
39. Anand L, Narayan S. 2019 An elastic-viscoplastic model for lithium. *J. Electrochem. Soc.* **166**, A1092–A1095. (doi:10.1149/2.0861906jes)
40. Mwizerwa JP, Liu C, Xu K, Zhao N, Li Y, Chen Z, Shen J. 2022 Three-dimensional printed lithium iron phosphate coated with magnesium oxide cathode with improved areal capacity and ultralong cycling stability for high performance lithium-ion batteries. *J. Colloid Sci.* **623**, 168–181. (doi:10.1016/j.jcis.2022.05.030)
41. Wang J, Sun Q, Gao X, Wang C, Li W, Holness F, Zheng M, Li R, Price A, Sun X. 2018 Toward high areal energy and power density electrode for Li-ion batteries via optimized 3D printing approach. *ACS Appl. Mater. Inter.* **10**, 39 794–39 801. (doi:10.1021/acsami.8b14797)
42. Liu Z, Tian X, Liu M, Duan S, Ren Y, Ma H, Tang K, Shi J, Hou S, Jin H, Cao G. 2021 Direct Ink Writing of $Li_{1.3}Al_{0.3}Ti_{1.7}(PO4)_3$-based solid-state electrolytes with customized shapes and remarkable electrochemical behaviors. *Small* **17**, 2002866. (doi:10.1002/smll.202002866)
43. Franco A. 2013 Multiscale modelling and numerical simulation of rechargeable Lithium ion batteries: concepts, methods and challenges. *RSC Adv.* **3**, 13 027–13 058. (doi:10.1039/c3ra23502e)
44. Tamilselvi S, Gunasundari S, Karuppiah N, Razak RKA, Madhusudan S, Nagarajan VM, Sathish T, Shamim MZM, Saleel CA, Afzal A. 2021 A review on battery modelling techniques. *Sustainability-Basel* **13**, 10042. (doi:10.3390/su131810042)
45. Gurtin M, Fried E, Anand L. 2010 *The mechanics and thermodynamics of continua*. Cambridge, UK: Cambridge University Press.
46. Arricca M, Cabras L, Serpelloni M, Bonanno C, McMeeking RM, Salvadori A. 2023 A coupled model of transport-reaction-mechanics with trapping, Part II: Large strain analysis. *J. Mech. Phys. Solids* **181**, 105425. (doi:10.1016/j.jmps.2023.105425)
47. Ganser M, Hildebrand F, Kamlah M, McMeeking R. 2019 A finite strain electro-chemo-mechanical theory for ion transport with application to binary solid electrolytes. *J. Mech. Phys. Solids* **125**, 681–713. (doi:10.1016/j.jmps.2019.01.004)
48. Serpelloni M, Salvadori A, Cabras L. 2026 A finite-strain chemo-electro-mechanical model for gel polymer electrolytes with dynamic ion exchange between fluid and polymer phases. *Eur. J. Mech. A/Solids* **117**, 105988. (doi:10.1016/j.euromechsol.2025.105988)

49. Simon A, Grzywna Z. 1992 On the Larché-Cahn theory for stress-induced diffusion. *Acta Metall. Mater.* **40**, 3465–3473. (doi:10.1016/0956-7151(92)90061-I)
50. Larche F, Cahn J. 1973 A linear theory of thermochemical equilibrium under stress. *Acta Metall Mater* **21**, 1051–1063.
51. Larche F, Cahn J. 1978 Non linear theory of thermochemical equilibrium under stress. *Acta Metall Mater* **26**, 53–60.
52. Zhao X, Hong W, Suo Z. 2008 Stretching and polarizing a dielectric gel immersed in a solvent. *Int. J. Solids Struct.* **45**, 4021–4031. (doi:10.1016/j.ijsolstr.2008.02.023)
53. Kovetz A. 1989 *The principles of electromagnetic theory*. Cambridge, UK: Cambridge University Press.
54. Kaiser T, Menzel A. 2021 A finite deformation electro-mechanically coupled computational multiscale formulation for electrical conductors. *Acta Mech.* **232**, 3939–3956. (doi:10.1007/s00707-021-03005-5)
55. Salvadori A, Grazioli D, Geers M, Danilov D, Notten P. 2015 A multiscale-compatible approach in modeling ionic transport in the electrolyte of (Lithium ion) batteries. *J. Power Sourc.* **293**, 892–911. (doi:10.1016/j.jpowsour.2015.05.114)
56. Salvadori A, Grazioli D, Magri M, Geers M, Danilov D, Notten P. 2015 On the role of saturation in modeling ionic transport in the electrolyte of (Li-ion) batteries. *J. Power Sourc.* **294**, 696–710. (doi:10.1016/j.jpowsour.2015.06.061)
57. Salvadori A, Bosco E, Grazioli D. 2014 A computational homogenization approach for Li-ion battery cells. Part 1 - Formulation. *J. Mech. Phys. Solids* **65**, 114–137. (doi:10.1016/j.jmps.2013.08.010)
58. Doyle M, Fuller T, Newman J. 1993 Modeling of galvanostatic charge and discharge of the Lithium/Polymer/Insertion cell. *J. Electrochem. Soc.* **140**, 1526–1533. (doi:10.1149/1.2221597)
59. Tadmor E, Miller R, Elliott R. 2011 *Continuum mechanics and thermodynamics: from fundamental concepts to governing equations*. Cambridge, UK: Cambridge University Press.
60. Prigogine I. 1977 Time, structure and fluctuations. Nobel Lecture.
61. Rajagopal KR, Srinivasa AR. 2004 On thermomechanical restrictions of continua. *Proc. R. Soc. A* **460**, 631–651. (doi:10.1098/rspa.2002.1111)
62. De Groot S, Mazur P. 1984 *Non-equilibrium thermodynamics*. New York (Mineola, NY): Dover.
63. Coleman BD, Gurtin ME. 2004 Thermodynamics with internal state variables. *J. Chem. Phys.* **47**, 597–613. (doi:10.1063/1.1711937)
64. Ván P. 2003 Weakly nonlocal irreversible thermodynamics. *ADP* **515**, 146–173. (doi:10.1002/andp.20035150302)
65. Holzapfel GA. 2000 *Nonlinear solid mechanics*, vol. 24. Chichester: Wiley.
66. McBride A, Bargmann S, Pond D, Limbert G. 2016 Thermoelastic modelling of the skin at finite deformations. *J. Therm. Biol.* **62**, 201–209. (doi:10.1016/j.jtherbio.2016.06.017)
67. Narayan S, Anand L. 2022 A coupled electro-chemo-mechanical theory for polyelectrolyte gels with application to modeling their chemical stimuli-driven swelling response. *J. Mech. Phys. Solids* **159**, 104734. (doi:10.1016/j.jmps.2021.104734)
68. Larsson J. 2007 Electromagnetics from a quasistatic perspective. *Am. J. Phys.* **75**, 230–239. (doi:10.1119/1.2397095)
69. Salvadori A, McMeeking R, Grazioli D, Magri M. 2018 A coupled model of transport-reaction-mechanics with trapping. Part I - small strain analysis. *J. Mech. Phys. Solids* **114**, 1–30. (doi:10.1016/j.jmps.2018.02.006)
70. Castellani E, Ismael J. 2016 Which Curie's principle? *Philos. Sci.* **83**, 1002–1013. (doi:10.1086/687933)
71. Serpelloni M, Arricca M, Bonanno C, Salvadori A. 2022 Chemo-transport-mechanics in advecting membranes. *Int. J. Eng. Sci.* **181**, 103746. (doi:10.1016/j.ijengsci.2022.103746)
72. Anand L. 2012 A Cahn-Hilliard-type theory for species diffusion coupled with large elastic-plastic deformations. *J. Mech. Phys. Solids* **60**, 1983–2002. (doi:10.1016/j.jmps.2012.08.001)
73. Yildiz E, Serpelloni M, Salvadori A, Cabras L. 2024 A comparative review of models for all-solid-state Li-Ion batteries. *Batteries* **10**, 150. (doi:10.3390/batteries10050150)
74. Fuller TF, Doyle M, Newman J. 1994 Simulation and optimization of the dual lithium ion insertion cell. *J. Electrochem. Soc.* **141**, 1. (doi:10.1149/1.2054684)
75. Luo J, Dai C, Wang Z, Liu K, Mao W, Fang D, Chen X. 2016 In-situ measurements of mechanical and volume change of $LiCoO_2$ lithium-ion batteries during repeated charge–discharge cycling by using digital image correlation. *Measurement* **94**, 759–770. (doi:10.1016/j.measurement.2016.09.023)

76. Lubarda VA. 2004 Constitutive theories based on the multiplicative decomposition of deformation gradient: thermoelasticity, elastoplasticity, and biomechanics. *AMR* **57**, 95–108. (doi:10.1115/1.1591000)
77. Cheng ZN, Wang GZ, Chen L, Wilde J, Becker K. 2000 Viscoplastic anand model for solder alloys and its application. *SSMT* **12**, 31–36. (doi:10.1108/09540910010331428)
78. Renganathan S, Sikha G, Santhanagopalan S, White RE. 2010 Theoretical analysis of stresses in a Lithium ion cell. *J. Electrochem. Soc.* **157**, 155–163. (doi:10.1149/1.3261809)
79. Danilov D, Niessen R, Notten P. 2011 Modeling all-solid-state Li-Ion batteries. *J. Electrochem. Soc.* **158**, A215–A222. (doi:10.1149/1.3521414)
80. Mendoza H, Roberts SA, Brunini VE, Grillet AM. 2016 Mechanical and electrochemical response of a licoo2 cathode using reconstructed microstructures. *Electrochim. Acta* **190**, 1–15. (doi:10.1016/j.electacta.2015.12.224)
81. Deng Z, Wang Z, Chu IH, Luo J, Ong SP. 2015 Elastic properties of alkali superionic conductor electrolytes from first principles calculations. *J. Electrochem. Soc.* **163**, A67. (doi:10.1149/2.0061602jes)
82. Cheng EJ, Taylor NJ, Wolfenstine J, Sakamoto J. 2017 Elastic properties of lithium cobalt oxide (LiCoO2). *J. Asian Ceram. Soc.* **5**, 113–117. (doi:10.1016/j.jascer.2017.03.001)
83. Liu G, Lu W. 2017 A model of concurrent lithium dendrite growth, SEI growth, SEI penetration and regrowth. *J. Electrochem. Soc.* **164**, A1826–A1833. (doi:10.1149/2.0381709jes)
84. Cabras L, Serpelloni M, Salvadori A. 2022 Electro-chemo-mechanics of solid state batteries with lithium plating and stripping. *Front. Mater.* **9**, 1052617. (doi:10.3389/fmats.2022.1052617)
85. Stolz L, Hochstädt S, Röser S, Hansen MR, Winter M, Kasnatscheew J. 2022 Single-ion versus dual-ion conducting electrolytes: the relevance of concentration polarization in solid-state batteries. *ACS Appl. Mater. Interfaces* **14**, 11559–11566. (doi:10.1021/acsami.2c00084)
86. Raijmakers L, Danilov D, Eichel RA, Notten P. 2020 An advanced all-solid-state Li-ion battery model. *Electrochim. Acta* **330**, 135147. (doi:10.1016/j.electacta.2019.135147)
87. Cabras L, Serpelloni M, Salvadori A. 2026 Data for: A thermodynamically consistent formulation for solid state batteries at finite strains. Zenodo. (doi:10.5281/zenodo.18648365)
88. Cabras L, Salvadori A, Serpelloni M. 2026 A thermodynamically consistent formulation for solid-state batteries at finite strains. Figshare. (doi:10.6084/m9.figshare.c.8351672)